DRAFT VERSION FEBRUARY 5, 2008
Preprint typeset using LaTeX style emulateapj v. 6/22/04

arXiv:astro-ph/0508085v1 2 Aug 2005

NUMERICAL GALAXY CATALOG -I. A SEMI-ANALYTIC MODEL OF GALAXY FORMATION WITH N-BODY SIMULATIONS

MASAHIRO NAGASHIMA,[1,2,3] HIDEKI YAHAGI,[3,4] MOTOHIRO ENOKI,[5,6] YUZURU YOSHII,[7,8] AND NAOTERU GOUDA[5]

Draft version February 5, 2008

ABSTRACT

We construct the *Numerical Galaxy Catalog* (νGC), based on a semi-analytic model of galaxy formation combined with high-resolution N-body simulations in a Λ-dominated flat cold dark matter (ΛCDM) cosmological model. The model includes several essential ingredients for galaxy formation, such as merging histories of dark halos directly taken from N-body simulations, radiative gas cooling, star formation, heating by supernova explosions (supernova feedback), mergers of galaxies, population synthesis, and extinction by internal dust and intervening H I clouds. As the first paper in a series using this model, we focus on basic photometric, structural and kinematical properties of galaxies at present and high redshifts. Two sets of model parameters are examined, strong and weak supernova feedback models, which are in good agreement with observational luminosity functions of local galaxies in a range of observational uncertainty. Both models agree well with many observations such as cold gas mass-to-stellar luminosity ratios of spiral galaxies, H I mass functions, galaxy sizes, faint galaxy number counts and photometric redshift distributions in optical pass-bands, isophotal angular sizes, and cosmic star formation rates. In particular, the strong supernova feedback model is in much better agreement with near-infrared (K'-band) faint galaxy number counts and redshift distribution than the weak feedback model and our previous semi-analytic models based on the extended Press-Schechter formalism. Observed Tully-Fisher relations for bright galaxies and color-magnitude relations for dwarf elliptical galaxies in clusters of galaxies are broadly reproduced, but no agreement with observations is obtained over whole ranges. Nevertheless, they are improved compared with results produced by other semi-analytic models. A direction for overcoming the remaining problems is discussed. We also find that the resolution of N-body simulations, which is down to $3 \times 10^9 M_\odot$ for the minimum mass of dark halos consisting of ten dark matter particles in our model, plays a significant role in galaxy formation, and that merging histories of dark halos directly taken from N-body simulations produce results different from models based on the extended Press-Schechter model even if the mass function of dark halos at present is set to be the same as that obtained by the same N-body simulations used here.

Subject headings: cosmology: theory – galaxies: evolution – galaxies: formation – large-scale structure of universe

1. INTRODUCTION

Galaxies are one of the most important hierarchies composing the Universe. For example, in order to understand the evolution of the Universe and its structure, galaxies are often used as a measure of space-time in performing wide-field or deep surveys. In the field of observational cosmology, therefore, galaxies are indispensable units in the Universe. What we should note about galaxies is, however, that galaxies have also been evolving along with the evolution of the Universe. Thus, correctly modeling the evolution of galaxies is essential in observational cosmology. At the same time, galaxies themselves are also interesting objects because many physical processes are involved in galaxy formation. However, since some processes such as star formation are still poorly understood, it has been challenging to understand galaxy formation. To attack this subject, correctly modeling galaxy formation is critical as well, particularly under the current situation that numerical hydrodynamical simulations of galaxy formation still have large uncertainties (see, e.g., Okamoto et al. 2003, 2005). Thus, the purpose of this paper is to construct a better and more reliable model of galaxy formation aided by high resolution N-body simulations, which are well established in contrast to hydrodynamical simulations of galaxy formation, with quality high enough to be compared with recent high precision observations.

It has been widely understood that the cold dark matter (CDM) model well describes the Universe. Recent high resolution observations such as those measuring anisotropies of the cosmic microwave background by the *Wilkinson Microwave Anisotropy Probe* (Spergel et al. 2003) and the type Ia supernova (SN) rate (e.g. Riess et al. 1998; Perlmutter et al. 1999) have revealed that the energy density in the Universe is dominated by dark energy or the cosmological constant, and that gravity is dominated by the CDM. The large-scale structure of the universe has evolved from small density fluctuations existing in the early universe via gravitational instability. Because the predicted amplitude of density fluctuations is monotonically increasing toward smaller scales,

Electronic address: masa@scphys.kyoto-u.ac.jp
[1] Department of Physics, Graduate School of Science, Kyoto University, Sakyo-ku, Kyoto 606-8502, Japan
[2] Department of Physics, University of Durham, South Road, Durham DH1 3LE, U.K.
[3] Division of Theoretical Astrophysics, National Astronomical Observatory, National Institute of Natural Science, Mitaka, Tokyo 181-8588, Japan
[4] Department of Astronomy, University of Tokyo, Bunkyo-ku, Tokyo 113-0033, Japan
[5] Division of Astrometry and Celestial Mechanics, National Astronomical Observatory, National Institute of Natural Science, Mitaka, Tokyo 181-8588, Japan
[6] Astronomical Data Analysis Center, National Astronomical Observatory, National Institute of Natural Science, Mitaka, Tokyo 181-8588, Japan
[7] Institute of Astronomy, School of Science, The University of Tokyo, Mitaka, Tokyo 181-0015, Japan
[8] Research Center for the Early Universe, School of Science, The University of Tokyo, Bunkyo-ku, Tokyo 113-0033, Japan

small-mass dark halos, which are virialized objects of dark matter, firstly collapse and then those of larger masses subsequently collapse swallowing the smaller dark halos. Therefore, the formation of cosmological structure predicted by the CDM model is often called the hierarchical clustering. Most baryonic processes, such as gas cooling and star formation, take place within dark halos because of the gravitational potential of dark matter. Therefore, galaxy formation models must be constructed within the framework of hierarchical clustering as a natural consequence of the CDM model.

Along this line, semi-analytic (SA) modeling of galaxy formation has been developed (e.g. Kauffmann, White & Guiderdoni 1993; Cole et al. 1994, 2000; van Kampen, Jimenez & Peacock 1999; Somerville & Primack 1999; Nagashima, Gouda & Sugiura 1999; Nagashima et al. 2001, 2002; Menci et al. 2002; Hatton et al. 2003). In most SA models, merging histories or *merger trees* of dark halos are realized by using a Monte Carlo method based on extended Press-Schechter (EPS) models (Peacock & Heavens 1990; Bond et al. 1991; Bower 1991; Lacey & Cole 1993; Kauffmann & White 1993; Somerville & Kolatt 1999; Cole et al. 2000) which provide mass functions of progenitor halos. The EPS formalism is an extension of the Press-Schechter (PS) model of mass functions of dark halos (Press & Schechter 1974), which are derived from the power spectrum of initial density fluctuations combined with a spherically symmetric collapse model to describe non-linear evolution of density fluctuations (Tomita 1969; Gunn & Gott 1972). Considering density fluctuations within an overdense region which collapses later, mass functions of progenitor halos of a larger, later collapsing halo are obtained. SA models also include several important physical processes such as gas cooling, star formation, heating by SN explosions (SN feedback) and galaxy mergers, which take place within dark halos. Moreover, to directly compare theoretical results with observations, a stellar population synthesis technique is usually incorporated. Because we do not follow the dynamics related with these processes as hydrodynamical simulations, the computation is much faster. This means that we can explore a much larger space of parameters characterizing these processes, and therefore SA modeling is an important approach, complementary to hydrodynamical simulations in understanding the physics of galaxy formation.

In addition to those galaxy formation processes, observations of high redshift galaxies suffer from several effects that are not intrinsic in galaxies. Baugh et al. (1998) and Nagashima et al. (2001, 2002) considered absorption of emitted light from high redshift galaxies by intervening H I clouds (Yoshii & Peterson 1994; Madau 1995). The latter work also took into account selection effects arising from cosmological dimming of surface brightness dependent on observations (Yoshii 1993; Totani & Yoshii 2000; Totani et al. 2001).

Furthermore, a new ingredient related to SN feedback has recently been introduced into an SA model by Nagashima & Yoshii (2004, hereafter NY04) for the first time. They considered dynamical response to starburst-induced gas removal from galaxies on the size and velocity dispersion (e.g. Yoshii & Arimoto 1987), followed by a change in the depth of the gravitational potential well. They also showed that the model can successfully explain many aspects of photometric, structural and kinematical properties of dwarf ellipticals. This is called the Mitaka model, and is the basis of the SA model we shall show in this paper.

The PS model, however, has been recognized to be consistent with N-body simulations only within a factor of two (Yano, Nagashima & Gouda 1996; Nagashima & Gouda 1997; Monaco 1998; Nagashima 2001; White 2002; Reed et al. 2003). Some SA models, therefore, use corrected mass functions based on high resolution N-body simulations (Sheth & Tormen 1999; Jenkins et al. 2001; Yahagi, Nagashima & Yoshii 2004) instead of the PS model. Benson et al. (2000, 2001) used information on halo distribution from an N-body simulation and adapted their SA models, GALFORM (Cole et al. 2000), in which an EPS model is used. This method has the virtue, not only of allowing spatial distribution of galaxies to be followed, but also of resolution to low-mass halos at high redshift being freely set from the N-body simulations. Unfortunately, we cannot avoid the limitations of the PS model with these approaches, because the problems of EPS formalism still remain. To bypass the limitations of EPS formalism, hybrid SA models have been developed in which merger trees of dark halos directly taken from N-body simulations are used, while we have to carefully interpret any results from such hybrid models because of the limited numerical resolution. Fortunately, currently available N-body simulations are of high enough resolution to resolve the effective Jeans mass after the cosmic reionization. This kind of hybrid model can also be used to derive spatial distributions of galaxies. Thus, combined with photometric properties, mock catalogs can be made for comparison with individual galaxy surveys, without any loss of SA model advantages. Therefore, this approach provides strong tools with which to study galaxy formation.

The pioneering work for this approach was carried out by Roukema et al. (1997). Since then, their work has been substantially improved upon by Kauffmann et al. (1999a,b), Diaferio et al. (1999, 2001), Somerville et al. (2001), Helly et al. (2003a,b), and Hatton et al. (2003). We have learned many things about the spatial clustering of galaxies, particularly of high redshift galaxies, from those models. However, as we shall show in this paper, those models suffer from limited numerical resolution of N-body simulations. As another direction to the extension of SA models with N-body simulations, we should note works by Okamoto & Nagashima (2001, 2003) and Springel et al. (2001), in which merging histories of *subhalos* in galaxy clusters are taken into account. This enables us to derive relationships between galaxy properties and spatial distribution in halos, such as the morphology-density relation (e.g. Dressler 1980). In this paper, we do not follow the merging histories of subhalos, but it would be worth including those in future.

In this paper, based on our previous work on the Mitaka SA model (NY04) and N-body simulations using a parallel adaptive mesh refinement (AMR) code (Yahagi 2005), we construct the *Numerical Galaxy Catalog* (νGC), which is an SA model combined with high resolution N-body simulations. As shown below, the mass resolution is high enough to resolve the Jeans mass, and the size of the simulation box is also large enough to express a fair sample of the universe. We refer the reader to Yahagi, Nagashima & Yoshii (2004), in which mass functions of dark halos are presented, to see how powerful this AMR N-body code is. As a first paper in a series of νGC, here we focus on photometric, structural and kinematical properties of galaxies at present and high redshift such as luminosity functions, cold gas fractions, sizes, the Tully-Fisher relation, faint galaxy number counts, redshift distributions, cosmic star formation histories, and so on. Spa-

TABLE 1
COSMOLOGICAL PARAMETERS

Ω_0	Ω_Λ	h	σ_8	$\Omega_{\rm b}$
0.3	0.7	0.7	0.9	0.048

NOTE. — Cosmological parameters are based on the *WMAP* results (Spergel et al. 2003).

tial distribution of galaxies is discussed in a subsequent paper (Yahagi et al. 2005). We also plan to extend this model in future (Enoki et al. 2005) to include a quasar formation model developed by Enoki, Nagashima & Gouda (2003) and Enoki et al. (2004).

This paper is outlined as follows: In §2 we describe our SA model. In §3 we summarize model parameters in our SA model. In §4 we compare the theoretical predictions of SA model galaxies with various observations at present. In §5 we examine high redshift galaxies predicted by our SA model with observations. In §6 we provide summary and conclusions.

2. MODEL

The galaxy formation scenario on which our model is based is as follows: In the CDM universe, small dark matter halos compared with typical present mass of halos emerge through non-linear gravitational evolution of small density fluctuations. Such dark halos cluster and merge into larger halos in a manner that depends on the adopted power spectrum of the initial density fluctuations. In each of the merged dark halos, radiative cooling of virialized hot gas, star formation, and gas reheating by supernovae occur. The cooled dense gas and stars constitute *galaxies*. Dark halos are filled with the virialized hot gas, so if the mass of halos is sufficiently large, it should be recognized as an intracluster medium. These galaxies sometimes merge in a common dark halo, and then more massive galaxies form. Repeating these processes, galaxies form and evolve to the present epoch.

Merging histories of dark halos are directly taken from N-body simulations (Yahagi, Nagashima & Yoshii 2004). The galaxy formation model running on the merging histories of dark halos is almost the same as the Mitaka model given by NY04, in which the merging histories were realized by using a Monte Carlo method based on the EPS formalism provided by Somerville & Kolatt (1999).

Some ingredients of our SA model are revised from those in NY04. Modifications include a model of the star formation (SF) time-scale, a prescription for mergers between satellite galaxies, and a dust extinction model during starbursts. The details are described below.

Throughout this paper, a recent standard ΛCDM model is considered, that is, $\Omega_0 = 0.3, \Omega_\Lambda = 0.7, h = 0.7$ and $\sigma_8 = 0.9$, where these parameters denote the mean density of the universe, the cosmological constant, the Hubble parameter and the normalization of the power spectrum of the initial density fluctuation field. The shape of the power spectrum given by Sugiyama (1995) is used, an extension of Bardeen et al. (1986) taking into account the effects of baryons. The cosmic baryon density $\Omega_{\rm b} = 0.048$ is adopted (Spergel et al. 2003). Those parameters are tabulated in Table 1. Model parameters described below are summarized in §3.

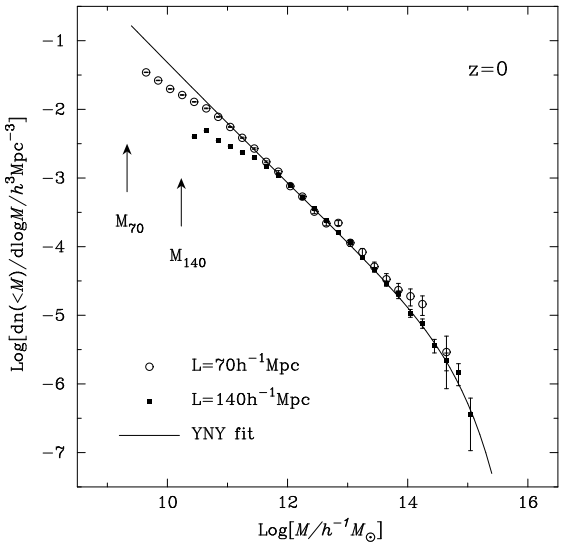

FIG. 1.— Mass functions of dark halos at $z = 0$. The open circles and solid squares with error bars represent mass functions given by the simulations of $L = 70h^{-1}$ Mpc and 140 h^{-1} Mpc, respectively. The error bars indicate 1 σ scatter. The minimum masses of those simulations are indicated by M_{70} and M_{140} in the figure. The solid line is a fitting function to results of several simulations (Yahagi, Nagashima & Yoshii 2004).

2.1. *N-body Simulations and Construction of Merging Histories of Dark Halos*

Merger trees of dark halos are directly taken from cosmological N-body simulations. Our simulation has $N = 512^3$ dark matter particles in a box size of $L = 70h^{-1}$Mpc. Since the minimum number of particles identifying a dark halo is 10, the minimum mass of dark halos M_{70} is nearly equal to $3.04 \times 10^9 M_\odot$. The simulation code is developed by Yahagi (2005), based on AMR technique to compute the gravitational force (Kravtsov et al. 1997; Knebe et al. 2001; Yahagi & Yoshii 2001; Teyssier 2002) with periodic boundary conditions. The method of identifying dark halos is the friends-of-friends (FoF) grouping algorithm (Davis et al. 1985), with the linking length $b = 0.2$ as usual.

Rigorously speaking, however, fully resolved mass might be larger, about $5 \times 10^{11} M_\odot$, at which the resultant mass function deviates from a power law, as indicated in Figure 1 by open circles with error bars. The solid line in the figure is a fitting function for several simulations performed with different box sizes from 35 to 140 h^{-1} Mpc proposed by Yahagi, Nagashima & Yoshii (2004). To evaluate the resolution effects on galaxy formation, we shall use another set of N-body results of a 140 h^{-1} Mpc box with the same number of particles, $N = 512^3$ in §§4.1. The mass function derived by this simulation is indicated in the figure by solid squares, with a minimum mass of $M_{140} = 8M_{70}$. Parameters of those two simulations, "70" and "140", are tabulated in Table 2.

Figure 2 shows the importance of examining the mass resolution of N-body simulations on galaxy formation. The solid lines indicate masses of dark halos for constant circular velocities, $V_{\rm circ}$ =20, 30, 40, 50, 60, 80, and 100 km s^{-1} as a function of redshift from the bottom to the top. We use the spherical collapse model to obtain the relationship between the mass and circular velocity, which is expressed as

$$M = 3.26 \times 10^6 \Delta(z)^{-1/2} \left(\frac{V_{\rm circ}}{\rm km\ s^{-1}} \right)^3 h^{-1} M_\odot, \qquad (1)$$

TABLE 2
PARAMETERS OF N-BODY SIMULATIONS

Simulation	L (h^{-1}Mpc)	N	Minimum Halo Mass ($M_\odot$)	b
70	70	512^3	$3.04 \times 10^9 (M_{70})$	0.2
140	140	512^3	$2.43 \times 10^{10} (M_{140})$	0.2

NOTE. — L is the size of the simulation box, N is the number of dark matter particles, and b is the linking length parameter for identifying isolated dark halos using the FOF algorithm. Particles within b times a mean separation of particles are grouped. The minimum halos are defined as those of 10 particles.

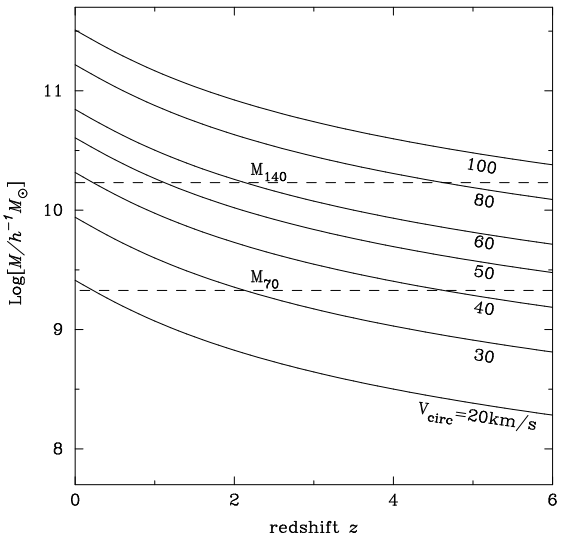

FIG. 2.— Relationship between mass and circular velocity of dark halos as a function of redshift. The solid lines indicate the mass of halos with constant circular velocities, $V_{\rm circ} = 20, ...100$ km s^{-1}, from the bottom to the top, as indicated in the figure. The dashed lines represent the minimum masses M_{70} and M_{140} of the simulations with 70 and $140h^{-1}$ Mpc box sizes, respectively.

where $\Delta(z)$ is the ratio of the mean density in halos collapsing at z to the critical density of the universe. The dashed lines are the minimum masses M_{70} and M_{140} as indicated in the figure.

After the cosmic reionization, the Jeans mass should be at least $V_{\rm circ} \simeq 20$ km s^{-1}, which corresponds to $T \simeq 10^4$ K. Based on his hydrodynamical simulations, Gnedin (2000) suggested that an effective Jeans mass, or the *filtering mass*, becomes even larger affected by the past thermal history, although the results for low redshifts were an extrapolation aided by a linear perturbation theory. Somerville (2002) has reported the following result on the effective Jeans mass: the mass of halos which retain half of the gas is well approximated by mass corresponding to circular velocity $V_{\rm circ} \simeq 50$ km s^{-1}; halos with $V_{\rm circ} < 30$ km s^{-1} are not able to accrete most of the gas and those with $V_{\rm circ} > 75$ km s^{-1} are almost unaffected. As shown in Figure 2, M_{70} corresponds to $V_{\rm circ} \simeq 20$ km s^{-1} at $z \simeq 0$ and 40 km s^{-1} at $z \simeq 5$. These values should be sufficient to resolve the effective Jeans mass. On the other hand, M_{140} corresponds to $V_{\rm circ} \simeq 40$ km s^{-1} at $z \simeq 0$ and 80 km s^{-1} at $z \simeq 5$. These are marginal, unless the effective Jeans mass is similar to or larger than that estimated by Gnedin (2000). Thus our 70 h^{-1}Mpc simulation is quite plausible for correct modeling of galaxy formation. Apart from detailed discussion on the Jeans mass, we shall study the effects of the resolution on luminosity functions in §§4.1. Note that other theoretical data in the public domain provided by SA models combined with N-body simulations have much larger masses of dark matter particles. For example, the particle mass in the GIF project (Kauffmann et al. 1999a) is about 65 times larger than ours, and that of the GalICS project (Hatton et al. 2003) is about 27 times larger. These masses are even larger than our 140 h^{-1} Mpc box simulation.

In our simulation, first collapsing halos emerge at $z \simeq 18$. Then we stock data sets of the particle distribution for approximately 70 time slices. When identifying dark halos, a marker particle for each halo is also defined, which is a particle whose mechanical energy is minimum. The marker particle is assigned to the halo's central galaxy, which is defined below. The position of galaxies is specified using the corresponding marker particles. A halo at time t_i is connected with another halo at the next time-step $t_{i+1} (> t_i)$ as its progenitor halo, which has the largest number of dark matter particles common to the both.

Some collapsed halos, especially small halos, disappear later. Such "floating" halos should be fake due to fluctuations of particle distribution, so we remove the floating halos from the sets of merger trees. Some collapsed halos sometimes fragment, particularly at low redshift. This is caused by highly dense clumps penetrating their host halos, which go back into and are absorbed by the host halos again later. To avoid such a "loop" structure in merging histories, the fragmented halos are forcedly merged into the host halos. Then each merger tree has a *tree structure* with a *root* halo at $z = 0$. Almost all fragmented halos are small and less than 10% of their host halos in mass. Because the resolution of our N-body simulation is very high, small halos swallowed by larger halos likely survive and penetrate. Physically, gas in such clumps should not fragment and should quickly merge into hot gas in their host halos, apart from dark matter, because gas is collisional different from collisionless dark matter. Therefore, as far as we focus on the evolution of baryons, this manipulation should be performed. The details of this simulation can be found in Yahagi (2005) and Yahagi, Nagashima & Yoshii (2004).

2.2. *Tidal Stripping of Subhalos*

Recent high resolution N-body simulations of galaxy clusters have revealed that swallowed dark halos survive in their host halos as *subhalos*. Envelopes of these subhalos are stripped by tidal force from the host halo. In our simulations, such subhalos are not identified but are taken into account by the following model. We assume the radius of a tidally stripped subhalo $r_{\rm t}$, which had a radius of $r_{\rm s}$ and mass of $M_{\rm s}$ before the stripping, by

$$\frac{r_{\rm t}}{r_{\rm s}} = \frac{r_{\rm peri}}{r_{\rm apo}} \frac{M_{\rm h}}{M_{\rm s}} \left(\frac{V_{\rm circ,s}}{V_{\rm circ,h}} \right)^3 , \qquad (2)$$

where $r_{\rm peri}$ and $r_{\rm apo}$ are respectively the pericenter and apocenter for the orbit of the subhalo, and subscripts "h" and "s" indicate the host halo and subhalo. In this paper, a ratio of $r_{\rm peri}/r_{\rm apo} = 0.2$ is assumed, as in NY04 (Okamoto & Habe 1999, 2000). Now we assume a singular isothermal distribution for dark matter in subhalos. This means that the decrease in mass by the tidal stripping is proportional to $r_{\rm t}/r_{\rm s}$. Thus, the tidal stripping significantly affects the time-scale of galaxy mergers (§§2.5).

2.3. *Hot Halo Gas and Its Cooling*

Firstly, we define the formation of halos as follows: Dark halos grow as time passes via mergers and accretion of other halos. Hereafter, the formation epoch of halos is referred to as the time when the mass of a dark halo exceeds twice the mass of the halo at the final formation epoch (Lacey & Cole 1993). At this time, the circular velocity of the halo is reestimated, since the halo is regarded as collapsing at this epoch. The mean mass density in dark halos is assumed to be proportional to the cosmic mean density at the formation epoch following the spherically symmetric collapse model, independent of the N-body results. Each collapsing dark halo contains baryonic matter with a mass fraction $\Omega_{\rm b}/\Omega_0$. The baryonic matter consists of diffuse hot gas, dense cold gas, and stars.

When a halo forms with a circular velocity $V_{\rm circ}$, the hot gas contained in the halo is shock-heated to the virial temperature of the halo,

$$T_{\rm vir} = \frac{1}{2}\frac{\mu m_{\rm p}}{k_{\rm B}} V_{\rm circ}^2, \tag{3}$$

where $m_{\rm p}, k_{\rm B}$ and μ are the proton mass, the Boltzmann constant, and the mean molecular weight. The hot gas density is assumed to have an isothermal density profile with a finite core radius, according to Shimizu et al. (2002),

$$\rho_{\rm hot}(r) = \frac{\rho_{\rm hot,0}}{1+(r/r_c)^2}, \tag{4}$$

where $r_c = 0.22 R_{\rm vir}/c$, $R_{\rm vir}$ is the virial radius of the host halo, and c is the concentration modeled by Bullock et al. (2001),

$$c(M,z) = \frac{9}{1+z}\left(\frac{M}{1.5\times10^{13}h^{-1}M_\odot}\right)^{-0.13}. \tag{5}$$

While in Cole et al. (2000), the concentration is altered depending on the history of each dark halo, we simply assume the above form of the concentration.

A part of the hot gas cools and accretes to the disk of a galaxy until subsequent collapse of dark halos containing this halo. The amount of the cooled gas is defined by the mass of the hot gas encircled by the *cooling radius*, at which the time elapsed from the formation epoch is equal to the cooling time-scale derived using the above density distribution,

$$t_{\rm cool}(r) = \frac{3}{2}\frac{\rho_{\rm hot}(r)}{\mu m_{\rm p}}\frac{k_{\rm B}T_{\rm vir}}{n_{\rm e}^2(r)\Lambda(T_{\rm vir}, Z_{\rm hot})}, \tag{6}$$

where $n_{\rm e}(r)$ are the electron density of hot gas at r, $Z_{\rm hot}$ is the metallicity of hot gas, and Λ is a metallicity-dependent cooling function provided by Sutherland & Dopita (1993). For simplicity, gas which cools in a time-step within a halo is added to cold gas of the central galaxy of the halo, which is defined in §§2.5, at the beginning of the time-step. Chemical enrichment in hot gas is consistently solved with star formation and SN feedback, as shown below.

In order to avoid the formation of unphysically large galaxies, the cooling process is applied only to halos with $V_{\rm circ} \leq V_{\rm cut}$. Although Cole et al. (2000) apparently succeeded in avoiding the formation of *monster galaxies* without such a cooling cut-off by introducing a history-dependent core radius, they have found that, in the case of higher baryon density, $\Omega_{\rm b} \simeq 0.04$, too many monster galaxies emerge (Benson et al. 2003). Here we take a simple approach to avoid the formation of monster galaxies, which is stopping cooling by hand. This will be solved if we treat heating processes in clusters of galaxies correctly, e.g. heating by AGN/QSOs. Throughout this paper, we set $V_{\rm cut} = 210$ km s^{-1}. This value might seem somewhat small. In addition to the higher baryon density, the reason for the difference of this kind of cooling cut-off from ones used in other recent SA models, in which $V_{\rm cut} \sim$ 350-500 km s^{-1} are used, is the treatment of reheated gas by SNe. For example, *superwinds* are adopted in Baugh et al. (2005) and Nagashima et al. (2005a) which expel gas by SNe in addition to the usual SN feedback. This frees us from the artificial cooling cut-off. However, the same model, but without the superwind, must adopt a small value of circular velocity for the cooling cut-off. Nagashima et al. (2005a) have reported that a model without the superwind requires $V_{\rm cut} = 100(1+z)^{3/4}$ km s^{-1}, where the redshift dependence originates by assuming heating by conductive heat fluxes from outer envelopes of halos. Thus, in the case of $\Omega_{\rm b} = 0.048$, under the assumption that all baryons are contained in halos, such a small $V_{\rm cut}$ is required. In future, mechanisms of gas-heating and of gas-expulsion from halos should be modeled.

The above assumption that all baryons are retained by dark halos might be too simple. Some have argued that gas known as the warm/hot intergalactic medium (WHIM) may be outside halos (e.g. Cen & Ostriker 1999; Yoshikawa et al. 2004; Nicastro et al. 2005). If the WHIM is the gas expelled from galactic-scale halos caused by the superwind or similar mechanisms, the baryon fraction in the halos is lowered. Instead, the WHIM might be the gas contained in smaller halos which are not resolved in hydrodynamical simulations (e.g. Inoue et al. 2004). Future observation of the WHIM will provide a clue to the baryon fraction in galactic-scale halos, which constrains the value of $V_{\rm cut}$.

2.4. *Star Formation and Supernova Feedback*

Stars in disks are formed from the cold gas. The SF rate (SFR) ψ is given by the cold gas mass $M_{\rm cold}$ and a SF time-scale τ_* as $\psi = M_{\rm cold}/\tau_*$. Although determining τ_* in a purely theoretical way is quite difficult, recent SA models suggest that τ_* should be dependent on characteristic velocities of galaxies and independent of redshift to explain many observations (Kauffmann & Haehnelt 2000; Nagashima et al. 2001, 2002; Enoki, Nagashima & Gouda 2003; Okoshi et al. 2004; Nagashima & Yoshii 2004; Baugh et al. 2005; Nagashima et al. 2005a). In this paper, we adopt a simple prescription, similar to that of Cole et al. (1994),

$$\tau_* = \tau_*^0 \left(\frac{V_d}{V_{\rm hot}}\right)^{\alpha_*}, \tag{7}$$

where τ_*^0 and α_* are free parameters, chosen to match the ratio of the cold gas mass to the B-band luminosity of spiral galaxies and V_d is the disk rotation velocity defined in §§2.6. $V_{\rm hot}$ is a parameter related to the SN feedback (see below). In NY04, the star formation time-scale was

$$\tau_* = \tau_*^0 \left[1+\left(\frac{V_d}{V_{\rm hot}}\right)^{-\alpha_{\rm hot}}\right], \tag{8}$$

where $\alpha_{\rm hot}$ is also a parameter related to the SN feedback defined below. Because this prescription has only one free parameter, τ_*^0, it is very helpful to search for suitable parameters. Although this worked well in NY04, in fact, we found that this cannot reproduce cold gas fractions in spiral galaxies in the case of weaker SN feedback.

Massive stars explode as Type II SNe and heat up the surrounding cold gas. This SN feedback reheats the cold gas at

a rate of $\dot{M}_{\rm reheat} = M_{\rm cold}/\tau_{\rm reheat}$, where the time-scale of reheating is given by

$$\tau_{\rm reheat} = \frac{\tau_*}{\beta(V_d)}, \tag{9}$$

where

$$\beta(V_d) \equiv \left(\frac{V_d}{V_{\rm hot}}\right)^{-\alpha_{\rm hot}}. \tag{10}$$

The free parameters $V_{\rm hot}$ and $\alpha_{\rm hot}$ are determined by matching the local luminosity function of galaxies with observations.

Below, we shall use two parameter sets. One of them has a strong SN feedback efficiency with $\alpha_{\rm hot} = 4$. This model is hereafter called the "strong feedback" (SFB) model. In this case, because of the strong SN feedback, we can take $\alpha_* = -\alpha_{\rm hot}$, which makes a star formation time-scale similar to NY04. It is not the case for a weak SN feedback. In the other model, the SN feedback is weak, $\alpha_{\rm hot} = 2$. This is called the "weak feedback" (WFB) model.

With the above equations and parameters, we obtain the masses of hot gas, cold gas, and disk stars as a function of time or redshift.

Associated with star formation and SN feedback, the chemical enrichment is also taken into account by extending Maeder (1992). For simplicity, instantaneous recycling is assumed for SNe II, and any contribution from SNe Ia is neglected. The recent progress on the chemical enrichment with SNe Ia in the framework of SA models is found in Nagashima & Okamoto (2004) and Nagashima et al. (2005a,b).

To sum up the above, the basic equations are

$$\dot{M}_* = \alpha\psi, \tag{11}$$

$$\dot{M}_{\rm cold} = -(\alpha+\beta)\psi, \tag{12}$$

$$\dot{M}_{\rm hot} = \beta\psi, \tag{13}$$

$$(M_{\rm cold}Z_{\rm cold})\dot{} = [p-(\alpha+\beta)Z_{\rm cold}]\psi, \tag{14}$$

$$(M_{\rm hot}Z_{\rm hot})\dot{} = \beta Z_{\rm cold}\psi, \tag{15}$$

where the dot ( ) indicates the time derivative, M_* and $M_{\rm hot}$ are the masses of stars and hot gas, respectively, $\psi = M_{\rm cold}/\tau_*$ is the SFR, α is a locked-up mass fraction which is set to be 0.75, consistent with a stellar evolution model we use, $Z_{\rm cold}$ and $Z_{\rm hot}$ are the metallicities of cold and hot gases, respectively, and p is the chemical yield which is set to be twice the solar metallicity in order to be consistent with the observed metallicity distribution of elliptical galaxies. We can solve these equations analytically as

$$\Delta M_{\rm cold}(t) = M^0_{\rm cold}\left\{1-\exp\left[-(\alpha+\beta)\frac{t}{\tau_*}\right]\right\}, \tag{16}$$

$$\Delta M_*(t) = \frac{\alpha}{\alpha+\beta}\Delta M_{\rm cold}(t), \tag{17}$$

$$\Delta M_{\rm hot}(t) = \frac{\beta}{\alpha+\beta}\Delta M_{\rm cold}(t), \tag{18}$$

$$Z_{\rm cold}(t) = Z^0_{\rm cold} + p\frac{t}{\tau_*}, \tag{19}$$

$$Z_{\rm hot}(t) = \Bigg[M^0_{\rm hot}Z^0_{\rm hot} + \frac{\beta}{\alpha+\beta}\Bigg\{ \left(\frac{p}{\alpha+\beta}+Z_{\rm cold}(t)\right)\Delta M_{\rm cold}(t) - (Z_{\rm cold}(t)-Z^0_{\rm cold})M^0_{\rm cold}\Bigg\}\Bigg]/M_{\rm hot}(t), \tag{20}$$

where variables with Δ indicate increments or decrements which are defined as positive and the superscript 0 stands for initial values at the beginning of the time-step, at which time t in the solutions is set at zero. For reference, we describe a mass-weighted mean stellar metallicity because it should be helpful to see the role of SN feedback on the chemical enrichment. The mass-weighted metallicity is given by

$$\langle Z_*(t)\rangle = \frac{\int_0^t \dot{M}_* Z_{\rm cold}(t)dt}{\int_0^t \dot{M}_* dt} = Z^0_{\rm cold} + \frac{p}{\alpha+\beta}\frac{1-e^{-u}-ue^{-u}}{1-e^{-u}}, \tag{21}$$

where $u \equiv (\alpha+\beta)t/\tau_*$. This means that when the SN feedback is strong, the increase in mean stellar metallicity is small. The SN feedback clearly plays an important role in chemical enrichment.

2.5. *Mergers of galaxies and formation of spheroids*

When two or more progenitor halos have merged, the newly formed larger halo should contain at least two or more galaxies which had originally resided in the individual progenitor halos. By definition, we identify the central galaxy in the new common halo with the central galaxy contained in the most massive of the progenitor halos. Other galaxies are regarded as satellite galaxies. These satellites merge either by dynamical friction or random collision. The time-scale of merging by dynamical friction is given by $\tau_{\rm mrg} = f_{\rm mrg}\tau_{\rm fric}$, where $\tau_{\rm fric}$ is given by Binney & Tremaine (1987),

$$\tau_{\rm fric} = \frac{1.17}{\ln\Lambda_{\rm C}}\frac{R_h^2 V_{\rm circ}}{GM_{\rm sub}}, \tag{22}$$

where R_h is the radius of the new common halo, $M_{\rm sub}$ is the mass of the tidally truncated subhalo, and $\Lambda_{\rm C}$ is the Coulomb logarithm. The parameter $f_{\rm mrg}$ is set to 0.8 in this paper by matching the bright end of luminosity functions. In order to judge whether or not a satellite merges with a central galaxy, we compute the time elapsed for each satellite galaxy since the galaxy becomes a satellite. This elapsed time is reset to zero if the mass of the host halo doubles. When the elapsed time exceeds $\tau_{\rm mrg}$, which is estimated from masses of the host halo and a tidally-stripped subhalo harboring the satellite, the satellite galaxy is accreted to the central galaxy.

Satellite galaxies sometimes merge in a time-scale of random collision. The merger rate, k, can be written using physical parameters of galaxies and their host halo,

$$k \sim n\sigma V_{\rm circ}, \tag{23}$$

where n is the number density of galaxies, and σ the cross section. Since the cross section is estimated from gravitational focusing, we can write $\sigma \propto (Gm_g/V^2_{\rm circ})^2$, where m_g is the mass of each galaxy. Using the virial relation, $m_g \simeq r_g v_g^2/G$, where r_g is the size of galaxies and v_g a characteristic velocity of galaxies, the merger rate is

$$k \propto \frac{N}{R_h^3}\frac{r_g^2 v_g^4}{V^3_{\rm circ}}, \tag{24}$$

where N is the number of galaxies in the halo. Makino & Hut (1997) derived a merger rate in a situation in which the mass of all galaxies was the same,

$$k_{\rm MH} = \frac{N}{500}\left(\frac{1{\rm Mpc}}{R_h}\right)^3\left(\frac{r_g}{0.1{\rm Mpc}}\right)^2 \times\left(\frac{\sigma_g}{100{\rm km\,s^{-1}}}\right)^4\left(\frac{300{\rm km\,s^{-1}}}{\sigma_h}\right)^3 {\rm Gyr}^{-1}, \tag{25}$$

where σ_g and σ_h are the one-dimensional velocity dispersions. Note that the *total* merger rate is $R_{\rm tot} = Nk_{\rm MH}$. Unless explicitly mentioned, we use this Makino-Hut merger rate for satellite-satellite mergers, as in Somerville & Primack (1999). After that, Mamon (2000) has proposed relaxing the assumption of equal-mass mergers in the following way: Consider a merger of galaxies with masses m and λm and assume $m \sim r_g^3$. Because k is considered to scale as $\langle r_g\rangle^2\langle v_g^2\rangle^2$, the rate should be

$$k(m,\lambda m) = k\left(\frac{1+\lambda^{1/3}}{2}\right)^2\left(\frac{1+\lambda^{2/3}}{2}\right)^2. \quad (26)$$

To introduce this into our model, the merger rate of a galaxy of mass m with galaxies of masses $\lambda_i m$, where i stands for other satellite galaxies in the same halo, is

$$\langle k(m)\rangle = \sum_i^{N-1}\frac{k(m,\lambda_i m)}{N}. \quad (27)$$

Later we shall see how this effect of non-equal mass mergers affects our results in Figure 10. In most of our results, however, we do not take into account this effect because it is almost negligible, at least at present, and because this requires quite a long time to compute. Below, we take $k_{\rm MH}$ as a fiducial merger rate, k, for equal-mass mergers, and use quantities of subhalos for the mass, radius and velocity dispersion of satellite galaxies. Here we define a collision timescale, $\tau_{\rm coll} = 1/\langle k\rangle$. With a probability $\Delta t/\tau_{\rm coll}$, where Δt is the time-step corresponding to the redshift interval Δz of merger trees of dark halos, a satellite galaxy merges with another satellite picked out randomly.

Consider the case when two galaxies of masses m_1 and $m_2(>m_1)$ merge. If the mass ratio $f = m_1/m_2$ is larger than a certain critical value of $f_{\rm bulge}$, we assume that a starburst occurs and that all of the cold gas turns into stars and hot gas according to the same SN feedback law, eq.(10), and all of the stars populate the bulge of a new galaxy. Note that when applying the SN feedback law, V_d is replaced by V_b defined in §§2.6, which is the velocity dispersion of the new bulge. The time-scale of the starburst is given by the dynamical time-scale, $\tau_* = r_e/V_b$, where r_e is the effective radius of the bulge, also defined in §§2.6. On the other hand, if $f < f_{\rm bulge}$, no starburst occurs, and a smaller galaxy is simply absorbed into the bulge of a larger galaxy. Note that in NY04 the smaller galaxy was absorbed into the disk of the larger galaxy. We have changed it to resemble the observed distribution of bulge-to-disk ratios of galaxies. Throughout this paper we use $f_{\rm bulge} = 0.3$, which gives a consistent morphological fraction in I_{814}-band galaxy number counts [see, e.g., Figure 13 in Nagashima et al. (2002)].

2.6. *Size of Galaxies and Dynamical Response to Starburst-induced Gas Removal*

Here we show a full description to estimate the size of galaxies, the rotation velocity of disks, and the velocity dispersion of bulges. The procedure is almost the same as that given by NY04 and shown schematically in Figure 3. A new parameter providing a fraction of energy dissipation during the major merger is introduced. It should be noted that the inclusion of the dynamical response to gas removal induced by starbursts provides much better agreement with observed kinematical and structural parameters, particularly for dwarf galaxies, as shown in NY04.

Dark halos have been considered to acquire angular momenta during the linear regime of their collapse through tidal torques made by the initial density fluctuation field (Peebles 1969; White 1984; Catelan & Theuns 1996a,b; Nagashima & Gouda 1998). Assuming that the hot gas component that cools and contracts within a dark halo has the same specific angular momentum as the dark halo has, we can estimate a radius at which the gas is supported by rotation with the conservation of its specific angular momentum. In this way, we determine the sizes of spiral galaxies.

In this model, angular momenta of dark halos are given by the following procedure, independent of the N-body results: This is not only for simplicity, but also because it is challenging at this stage to deal with the change in direction of the angular momentum, which is neglected here as usually assumed. The distribution of the dimensionless spin parameter $\lambda_{\rm H}$, which is defined by $\lambda_{\rm H} \equiv L|E|^{1/2}/GM^{5/2}$ where L is the angular momentum and E is the binding energy, is well approximated by a log-normal distribution (Mo, Mao & White 1998),

$$p(\lambda_{\rm H})d\lambda_{\rm H} = \frac{1}{\sqrt{2\pi}\sigma_\lambda}\exp\left[-\frac{(\ln\lambda_{\rm H}-\ln\bar{\lambda})^2}{2\sigma_\lambda^2}\right]d\ln\lambda_{\rm H}, \quad (28)$$

where $\bar{\lambda}$ is the mean value of the spin parameter and σ_λ is its logarithmic variance. We adopt $\bar{\lambda} = 0.05$ and $\sigma_\lambda = 0.5$ according to Mo, Mao & White (1998). When the angular momentum of the hot gas is conserved, the effective radius r_e of a resultant cold gas disk is related to the initial radius R_i of the hot gas sphere via $r_e = (1.68/\sqrt{2})\lambda_{\rm H}R_i$ (Fall 1979; Fall & Efstathiou 1980; Fall 1983). The initial radius R_i is set to be the smaller of the virial radius of the host halo and the cooling radius. A galaxy disk grows due to cooling and accretion of hot gas from the more distant envelope of its host halo. In our model, the disk size of each central galaxy is estimated at each time-step by the above method, but it is not always renewed. Only when both mass and estimated size of each disk are larger than those in the previous time-step, the size is renewed. At this time, the disk rotation velocity V_d is set to be the circular velocity of its host dark halo.

Size estimation of high-redshift spiral galaxies, however, carries uncertainties because of the large dispersion in their observed size distribution. For example, Simard et al. (1999) suggests only mild evolution of disk size against the redshift, taking into account the selection effects arising from the detection threshold of surface brightness, although the above simple model predicts disk size proportional to virial radius $R_{\rm vir}$ of host dark halos evolving as $R_{\rm vir} \propto 1/(1+z)$ for a fixed mass. Allowing for the possibility that the conservation of the angular momentum is not complete and/or for other sources such as the SN feedback to stop the contraction of gas disks, we generalize this size estimation by introducing a simple redshift dependence,

$$r_e = \frac{1.68}{\sqrt{2}}\lambda_{\rm H}R_i(1+z)^\rho, \quad (29)$$

where ρ is a free parameter. We simply use $\rho = 1$ as a reference value in this paper in order to be consistent with the observational galaxy number counts. The changing of the value of ρ affects the selection effects due to the cosmological dimming of surface brightness and the dust extinction, because the dust column density also changes with galaxy size.

In the case of the formation of elliptical galaxies driven by major mergers of galaxies, the size and velocity dispersion

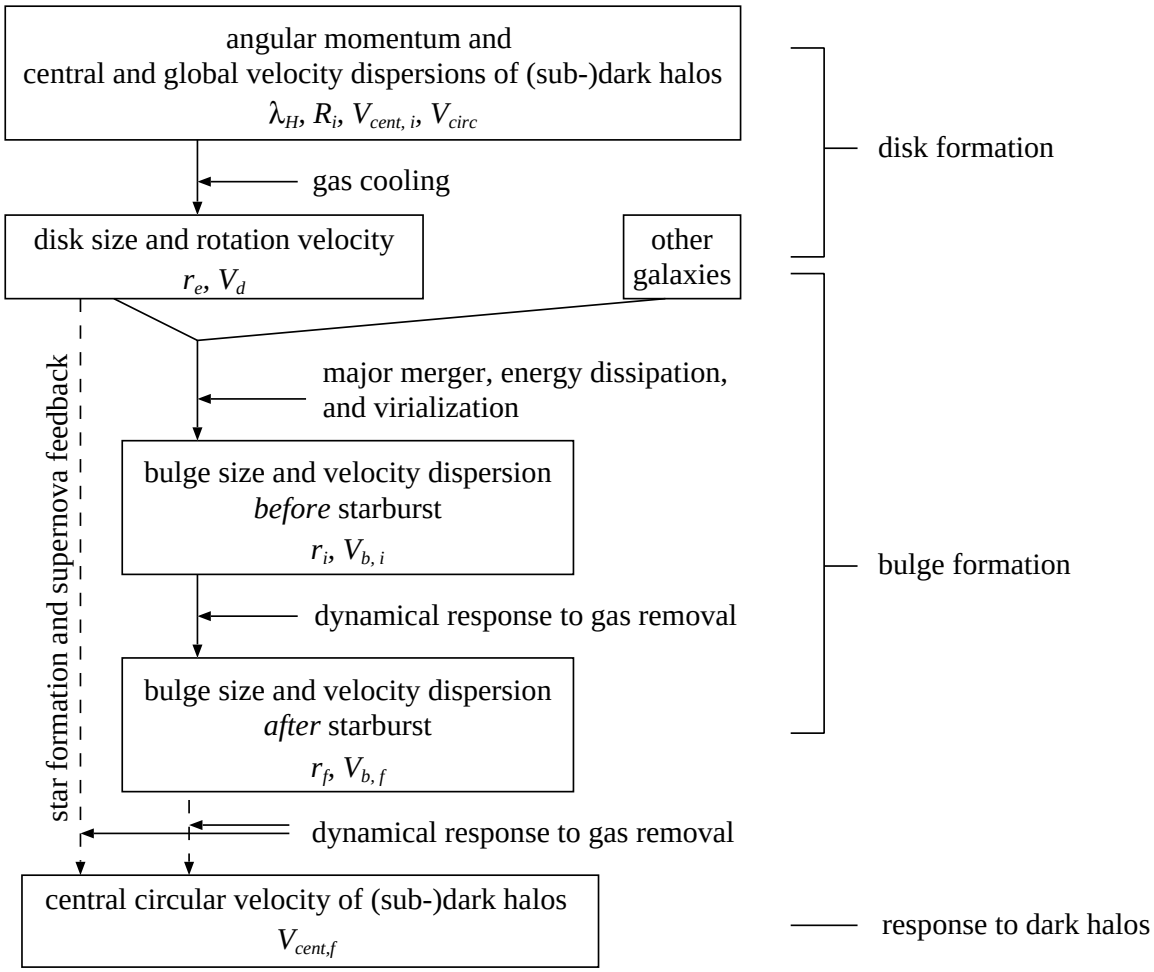

FIG. 3.— Diagram showing the flow to estimate sizes and velocities of dark halos, disks, and bulges.

are estimated, explicitly taking into account the dynamical response to starburst-induced gas removal. The outline is as follows: At first, two or more galaxies merge. During the merger, a fraction $f_{\rm diss}$ of the total energy of baryonic matter is assumed to be dissipated and a spheroidal merger remnant is formed and reaches the virial equilibrium immediately. Subsequently, the starburst occurs and a fraction of gas is gradually expelled from the spheroidal system according to the SN feedback law. Because the gravitational potential varies during the gas removal, the system expands and its velocity dispersion is lowered. The detail is shown below.

Sizes of early-type galaxies are primarily determined by the virial radius of the baryonic component. When a major merger of galaxies occurs, assuming some fraction of the energy loss to the total energy and no rotation of the merger remnant, we estimate the velocity dispersion of the merged system. Now we assign the subscript 0 to the merged galaxy, and subscripts 1 and 2 to the central and satellite galaxies, respectively, in the case of central-satellite merger, or to larger and smaller galaxies, respectively, in the case of satellite-satellite merger. Using the virial theorem, the total energy for each galaxy is

$$E_i = -\frac{1}{2}[M_b V_b^2 + (M_d + M_{\rm cold})V_d^2], \tag{30}$$

where M_b and M_d are the masses of bulge and disk stars, respectively, and V_b and V_d are the velocity dispersion of bulge and the rotation velocity of disk, respectively. Assuming the virial equilibrium, the binding energy E_b between the progenitors just before the merger is given by

$$E_b = -\frac{E_1 E_2}{(M_2/M_1)E_1 + (M_1/M_2)E_2}. \tag{31}$$

Then we obtain

$$f_{\rm diss}(E_1 + E_2 + E_b) = E_0, \tag{32}$$

where $f_{\rm diss}(\geq 1)$ is a parameter which describes how large a fraction is dissipated from the system. Just after the merger, there remains only the bulge component consisting of cold gas and stars in the merger remnant, whose velocity dispersion is directly estimated from the above equation. Then the size of the system just after the merger is defined by

$$r_i = \frac{GM_i}{2V_b^2}, \tag{33}$$

where $M_i = M_* + M_{\rm cold}$ is the total baryonic mass of the merged system. In reality, the rate of energy dissipation depends on complicated physical processes such as the escape of high velocity stars and the viscosity and friction due to gas. Throughout this paper, however, we adopt $f_{\rm diss} = 1.3$ for simplicity, which is chosen so that the size and velocity dispersion

of ellipticals agrees with observations. Apart from $f_{\rm diss}$, this way of estimating V_b and r_i is similar to that adopted in other SA models such as that by Cole et al. (2000), in which they formulate the conservation of energy in terms of the size.

Next, the cold gas turns into stars and hot gas. Since part of the gas is expelled from galaxies to halos due to the SN feedback, the mass of the system changes. Assuming the density distributions of baryonic and dark matters, the dynamical response on the structural parameters to the mass loss can be estimated. This process was taken into account for the first time in the Mitaka model (NY04) in the framework of SA modeling. In this paper we adopt the Jaffe model (Jaffe 1983) for baryonic matter and the static singular isothermal sphere for dark matter, and assume slow (adiabatic) gas removal compared with the dynamical time-scale of the system. Note that Nagashima & Yoshii (2003) also show the dynamical response for different density distributions of baryonic and dark matter and for rapid gas removal cases. Defining by $\mathcal{M}, R, Y$ and U the ratios of mass, size, density and velocity dispersion at a final state relative to those at an initial state, the response under the above assumption is approximately given by

$$R \equiv \frac{r_f}{r_i} = \frac{1 + D/2}{\mathcal{M} + D/2}, \tag{34}$$

$$U \equiv \frac{V_{b,f}}{V_{b,i}} = \sqrt{\frac{YR^2 + Df(z_f)/2}{1 + Df(z_i)/2}}, \tag{35}$$

where $\mathcal{M} = YR^3$, $D = 1/y_i z_i^2$, y and z are the ratios of density and size of baryonic matter to those of dark matter and, $f(z)$ is

$$f(z) = \frac{\ln(1+z)}{z} + \ln\left(1 + \frac{1}{z}\right). \tag{36}$$

The subscripts i and f stand for the initial and final states in the mass loss process. The contribution of dark matter is estimated from the central circular velocity of halos, $V_{\rm cent}$, which is defined below. According to numerical simulations of starbursts performed by Mori et al. (1997) and Mori, Yoshii & Nomoto (1999), the time-scale of gas removal might be comparable to the dynamical time-scale for dwarf ellipticals. If the gas-removal is almost instantaneous, the effect of the dynamical response becomes stronger, as shown by Nagashima & Yoshii (2003). Therefore, the assumption of the slow gas removal is conservative. In reality, some galaxies might become gravitationally unbound due to the rapid gas-removal. Stars of such galaxies should contribute to halo stars or intracluster stars.

Finally the back reaction to the gas removal by the SN feedback on dark matter distribution is computed. It is natural to consider that dark matter distribution in the central region of dark halos is also affected by the dynamical response to gas removal, because baryons usually condense with density comparable to that of dark matter. To take into account this process, we define a central circular velocity of dark halo $V_{\rm cent}$. When a dark halo collapses without any progenitors, $V_{\rm cent}$ is set to $V_{\rm circ}$. After that, although the mass of the dark halo grows by subsequent accretion and/or mergers, $V_{\rm cent}$ remains constant or decreases with the dynamical response. When the mass is doubled, $V_{\rm cent}$ is set to $V_{\rm circ}$ again. The dynamical response to mass loss from a central galaxy of a dark halo by SN feedback lowers $V_{\rm cent}$ of the dark halo as follows:

$$\frac{V_{{\rm cent},f}}{V_{{\rm cent},i}} = \frac{M_f/2 + M_d(r_i/r_d)}{M_i/2 + M_d(r_i/r_d)}. \tag{37}$$

The change of $V_{\rm cent}$ in each time-step is only a few per cent. Under these conditions, the approximation of static gravitational potential of dark matter is valid during starbursts. This also applies to subhalos.

Once a dark halo falls into its host dark halo, it is treated as a subhalo. Because we assume that subhalos do not grow in mass, the central circular velocity of the subhalos monotonically decreases. Thus, this affects the dynamical response later when mergers between satellite galaxies occur. We assume that the resultant density distribution remains isothermal with $V_{\rm cent}$ at least within the galaxy size.

The details of the dynamical response are shown in Nagashima & Yoshii (2003, 2004). The effect of the dynamical response is the most prominent for dwarf galaxies of low circular velocity because of the substantial removal of gas due to strong SN feedback (Yoshii & Arimoto 1987; Nagashima & Yoshii 2004). If the dynamical response had not been taken into account, velocity dispersions of dwarf ellipticals would have been much larger than those of observations, determined only by circular velocities of small dark halos in which dwarf ellipticals resided. For giant ellipticals, on the other hand, the effect of the dynamical response is negligible because only a small fraction of gas can be expelled due to weak SN feedback. We refer the reader to NY04 for detailed discussion of the dynamical response.

2.7. *Photometric Properties and Morphological Identification*

The above processes are repeated until the output redshift and then the SF history of each galaxy is obtained. For the purpose of comparison with observations, we use a stellar population synthesis approach, from which the luminosities and colors of model galaxies are calculated. Given the SFR as a function of time or redshift, the absolute luminosity and colors of individual galaxies are calculated using a population synthesis code by Kodama & Arimoto (1997). The stellar metallicity grids in the code cover a range from Z_* =0.0001 to 0.05. Note that we now define the metallicity as the mass fraction of metals. The initial stellar mass function (IMF) that we adopt is the power-law IMF of Salpeter form (Salpeter 1955), with lower and upper mass limits of $0.1M_\odot$ and $60M_\odot$, respectively. In some SA models, it has been assumed that there is a substantial fraction of invisible stars such as brown dwarfs which have masses smaller than $0.1M_\odot$. In this paper, however, we do not assume any contributions of such invisible stars to the stellar mass according to NY04.

The optical depth of internal dust is consistently estimated by our SA model. We make the usual assumption that the abundance of dust is proportional to the metallicity of cold gas, and the optical depth is proportional to the column density of metals. Then the optical depth τ is given by

$$\tau \propto \frac{M_{\rm cold} Z_{\rm cold}}{r_e^2}(1+z)^{-\gamma}, \tag{38}$$

where r_e is the effective radius of galaxies and γ is a free parameter which should be chosen to predict high redshift galaxies being consistent with observations. There are large uncertainties in estimating the proportionality constant, but we adopt about half the value used by Cole et al. (2000) according to NY04, because it predicts too strong an extinction to reproduce galaxy number counts. Wavelength dependence of optical depth is assumed to be the same as the Galactic extinction curve given by Seaton (1979). Dust

distribution is simply assumed to obey the slab dust model (Disney, Davies & Phillipps 1989) for disks, according to our previous papers.

In this paper, we introduce dust extinction during starbursts. We randomly assign the merger epoch within a time-step under consideration, according to the time-scale of mergers. The SF time-scale of the bursting galaxy is assumed to be the dynamical time-scale, r_e/V_b. This time-scale enables us to compute the amount of metals in cold gas at the output redshift or the end of the time-step. Assuming the screen dust model, the optical depth is estimated. This procedure is important to obtain consistency with observational colors of high redshift galaxies. If we do not include this, some galaxies right after major mergers become too blue to be consistent with observations. This is discussed in §§5.4.

The origin of γ is still unknown. We have introduced this parameter just as a phenomenological one. In the WFB model, we set $\gamma = 0$, but in the SFB model $\gamma = 1$ to decrease the optical depth at high redshift, otherwise too few galaxies were formed to reconcile with observed galaxy number counts. One of the reasons this is required is that the dust-to-gas ratio may evolve with redshift. At high redshift, the ratio might be lower than at low redshift. Another possible reason is that the chemical yield we adopt is nearly equal to twice the solar value, which might be too large. This large value is required to be consistent with observed colors of cluster elliptical galaxies, which have been considered to have shallower IMFs of stars than disk stars, so that the chemical yield may be larger than the solar (Arimoto & Yoshii 1986, 1987). If this is true, the value of the chemical yield must be different depending on the environment, that is, the yield for disk stars should be approximately solar, but larger than solar for spheroidal components. Because γ is required to decrease the optical depth of dust in disks, by adopting a chemical yield similar to the solar value, we will be able to set $\gamma = 0$. As for recent progress in investigating the chemical enrichment using SA models, we refer the reader to Nagashima & Okamoto (2004), Baugh et al. (2005) and Nagashima et al. (2005a). In this paper, we do not enter into any details and maintain γ as a phenomenological parameter to reproduce observed high redshift galaxies.

Light emitted from high redshift galaxies is also absorbed by intergalactic H I clouds. We include this effect in our SA model, according to Yoshii & Peterson (1994) (see also Madau 1995; Madau et al. 1996). The optical depth for a source at redshift z_s at a wavelength λ is written as

$$\tau_\lambda(z_s) = \int_0^{z_s}\int_0^\infty dW \frac{\partial^2\mathcal{N}}{\partial z \partial W}\left\{1 - e^{-s[(1+z)\nu]N(W)}\right\}, \tag{39}$$

where $\nu = c/\lambda$, $\partial^2\mathcal{N}/\partial z\partial W$ is the number of the Lyα lines per unit interval redshift per rest-frame Lyα equivalent width W, $N(W)$ is the hydrogen column density which is related to W through the curve of growth for the Lyα absorption line, and $s(\nu)$ is the sum of absorption cross sections for the lines and continuum of the hydrogen atom dependent on the Doppler b-parameter, which is assumed to be $b = 20$ km s^{-1}. The cross sections for the lines and the continuum are expressed as

$$s_{nn'}(\nu) = \frac{\pi e^2}{m_e c} f_{nn'} \times \int_{-\infty}^{\infty} \frac{(\Gamma_{n'}/4\pi^2)e^{-v^2/b^2}dv}{\sqrt{\pi}b\{[\nu_{nn'} + (v/c)\nu_{nn'} - \nu]^2 + (\Gamma_{n'}/4\pi^2)\}} \tag{40}$$

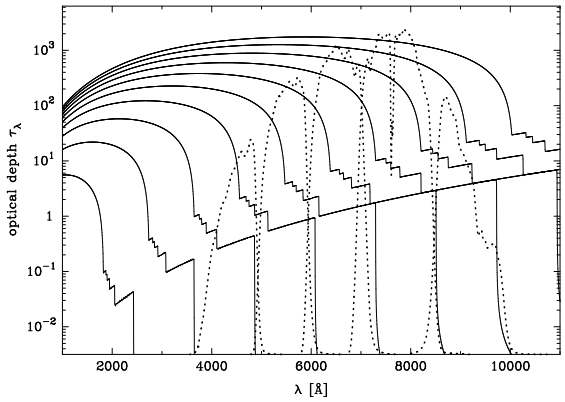

FIG. 4.— Optical depth as a function of observed wavelength for various source redshifts, $z_s = 1, 2, ...10$ from the left to the right. Response functions of $BVRi'z'$ bands for the Suprime-Cam on the Subaru telescope are overlaid by the dotted lines from the left to the right. Note that the vertical axis for these is in linear scale.

and

$$s_n(\nu) = \frac{64\pi^4 m_e e^{10} g_n(\nu)}{3\sqrt{3}ch^6 n^5 \nu^3} \times \int_{-\infty}^{\infty} \frac{\{1 - \theta[\nu_n + (v/c)\nu_n - \nu]\}e^{-v^2/b^2}dv}{\sqrt{\pi}b}, \tag{41}$$

where $\theta(x)$ is the Heaviside step function, $\Gamma_{n'}$ is the effective damping constant, $g_n(\nu)$ is the Gaunt factor, and the other notations have their usual meanings. We consider Lyman continuum absorption ($n = 1$) and the first five lines of Lyman series, Lyα, ... Lyϵ ($n = 1$ and $n' = 2, ...6$). The line distribution can be modeled as

$$\frac{\partial^2\mathcal{N}}{\partial z \partial W} = 10.7(1+z)^{2.37}\frac{e^{-W/W^*}}{W^*}, \tag{42}$$

where $W^* = 0.36$Å, according to the Model I in Yoshii & Peterson (1994). Combined with response functions of the filters we use, we obtain the optical depths for individual pass-bands. We simply estimate an optical depth for an X-band, τ_X, as

$$\exp(-\tau_X) = \frac{\int d\lambda R_{X,\lambda} e^{-\tau_\lambda}}{\int d\lambda R_{X,\lambda}}, \tag{43}$$

where $R_{X,\lambda}$ is a response function to the X-band filter. The difference in magnitudes is given by $\Delta m = 2.5\tau_X \log e$. Figure 4 shows the optical depths at $z_s = 1, ...10$, indicated by the solid lines, and response functions of $BVRi'z'$ of the *Subaru* telescope by the dotted lines, which are used in §5.

We classify galaxies into different morphological types according to the B-band bulge-to-disk luminosity ratio B/D. In this paper, following Simien & de Vaucouleurs (1986), galaxies with $B/D \geq 1.52$, $0.68 \leq B/D < 1.52$, and $B/D < 0.68$ are classified as elliptical, lenticular, and spiral galaxies, respectively. Kauffmann, White & Guiderdoni (1993) and Baugh, Cole & Frenk (1996) showed that this method of type classification well reproduces the observed type mix.

Luminosity profiles of galaxies are assumed to obey the de Vaucouleurs' 1/4 law for E/S0 galaxies and the exponential law for spirals. These profiles are used to compute the isophotal magnitude, which is obtained by integrating light from the galactic center to a radius at which the surface brightness reaches a threshold value. If the threshold is smaller in units

TABLE 3
ASTROPHYSICAL PARAMETERS

Parameter	SFB	WFB	Annotation	Observation
$\alpha_{\rm hot}$	4	2	supernova feedback-related (§§2.3)	luminosity functions (Figure 7)
$V_{\rm hot}$ (km s^{-1})	140	140		
$V_{\rm cut}$ (km s^{-1})	210	210	cooling cut-off (§§2.3)	luminosity functions (Figure 7)
α_*	-4	-2.3	star formation-related (§§2.4)	cold gas mass (Figure 11)
τ_*^0(Gyr)	2.4	2		
$p\,(Z_\odot)$	2	2	heavy-element yield (§§2.4)	metallicity distribution (not shown)
$f_{\rm bulge}$	0.3	0.3	major/minor merger criterion (§§2.5)	morphological counts (not shown)
$f_{\rm mrg}$	0.8	0.8	coefficient of dynamical friction timescale (§§2.5)	luminosity functions (Figure 7)
$f_{\rm diss}$	1.3	1.3	energy-loss fraction (§§2.6)	spheroidal size (Figure 14) and velocity dispersion (Figure 16)
$\bar{\lambda}$	0.03	0.03	spin parameter distribution (§§2.6)	disk size (Figure 13)
σ_λ	0.5	0.5		
ρ	1	1	redshift dependence of disk size (§§2.6)	faint galaxy number counts (Figures 18, 19 and 23)
γ	1	0	redshift dependence of dust optical depth (§§2.7)	faint galaxy number counts (Figures 18, 19 and 23)

NOTE. — $\alpha_{\rm hot}$ and $V_{\rm hot}$ are the SN feedback-related parameters (eq. 10). α_* and τ_*^0 are the SFR-related parameters (eq. 7). $f_{\rm bulge}$ is a critical mass-ratio of merging galaxies to distinguish major and minor mergers (§§2.5). $f_{\rm mrg}$ is a parameter to fine-tune the time-scale of mergers due to dynamical friction (§§2.5). p is the chemical yield as defined by Maeder (1992) (eq. 14). $\bar{\lambda}$ and σ_λ characterize the distribution function of the dimensionless spin parameter, $\lambda_{\rm H}$, with a shape of log-normal type (eq. 28). Their values are given by Mo, Mao & White (1998). ρ is a parameter giving a redshift dependence of the disk size (eq. 29). $f_{\rm diss}$ represents the energy-loss to the total energy during the major merger (eq. 32). γ is a parameter giving a redshift dependence of dust optical depth (eq. 38). The last column denotes observational quantities which are used to set the values of the parameters of the model.

of surface brightness, e.g., mag arcsec^{-2}, the contribution to the isophotal magnitude comes only from the central region of the galaxy. Where the threshold is infinity, the isophotal magnitude is identical to the total magnitude. Thus, the threshold depends on the depth of observations. It is very important for high redshift galaxies to estimate the isophotal magnitude because of the selection effects for detection. The details of how to compute the isophotal magnitude are shown in Yoshii (1993), Totani & Yoshii (2000) and Totani et al. (2001), and in Nagashima et al. (2001, 2002) in the framework of SA models.

3. MODEL PARAMETERS

Here we briefly summarize model parameters. As already mentioned, we adopt a standard ΛCDM model. The cosmological parameters are $\Omega_0 = 0.3, \Omega_\Lambda = 0.7, h = 0.7$ and $\sigma_8 = 0.9$, and the baryon density parameter is $\Omega_{\rm b} = 0.048$, as tabulated in Table 1, suggested by the first-year *WMAP* results (Spergel et al. 2003). The shape of the power spectrum of density fluctuations adopted here is that of Sugiyama (1995), in which the effects of baryons are taken into account to improve the power spectrum given by Bardeen et al. (1986).

Most of the astrophysical parameters are constrained from local observations, according to the procedure discussed in Nagashima et al. (2001, 2002) and NY04. The values adopted are slightly different from those in our previous papers. This is mainly caused by different merger trees which are directly constructed in this paper using N-body simulations. We shall show that correctly constructing merger trees is very important in §§4.1. In the Mitaka model (NY04), we used a mass function which fits with results of the N-body simulations we used here (Yahagi, Nagashima & Yoshii 2004), which means that mass functions of dark halos are the same at output redshift, e.g. at $z = 0$. However, we have found that luminosity functions in this model are different from those in NY04, in which an extended Press-Schechter model was used to construct merger trees (see Figure 9). This shows that merger trees of dark halos directly affect properties of galaxies.

Parameters are determined in the following way: Firstly, the SN feedback-related parameters, $\alpha_{\rm hot}$ and $V_{\rm hot}$ are constrained by matching luminosity functions (see Figure 7). Roughly speaking, $\alpha_{\rm hot}$ determines the faint-end slope and $V_{\rm hot}$ the magnitude of L^* galaxies. Since observational uncertainties in estimating luminosity functions still remain, we have a degree of freedom in varying those parameters. In the Mitaka model, we have used $\alpha_{\rm hot} = 4$, a parameter also used in this paper and referred to as the SFB model. In many other SA models, however, $\alpha_{\rm hot} = 2$ is often used (e.g. Kauffmann, White & Guiderdoni 1993; Somerville & Primack 1999; Cole et al. 2000). Therefore, we provide another parameter set, the WFB model, with $\alpha_{\rm hot} = 2$. $V_{\rm hot}$ is determined for luminosity functions to be consistent with observations under the constraint of $\alpha_{\rm hot}$. Second, SFR-related parameters, τ_*^0 and α_*, are determined by matching cold gas fractions in spiral galaxies, $M_{\rm HI}/L_B$ (see Figure 11). As mentioned, we have found that $\alpha_* = -\alpha_{\rm hot}$ for the SFB model, but $\alpha_* = -2.3$ for the WFB model, which is slightly different from $-\alpha_{\rm hot} = -2$. Finally, other parameters such as the mean spin parameter are fine-tuned, but they are quite similar to physically motivated values. The values of these parameters are tabulated in Table 3.

Figure 5 shows the projected density distribution of dark matter taken from the $L = 70h^{-1}$ Mpc simulation at six different redshifts from $z = 0$ to 5. It is evident that dark matter is clustering more as time passes. Figure 6 shows the same distribution as Figure 5 but for galaxies of $M_B \leq -19.5$ ($M_B - 5\log h \lesssim -18.7$) in the rest frame. The position of galaxies is specified by the marker particles, as mentioned in §§2.1. Sizes and colors of symbols represent the rest frame magnitudes and colors of galaxies, respectively. In this plot, we do not take into account the selection effects and absorption of light by intergalactic H I clouds. At higher redshifts, galaxies become bluer. By contrast, clustering properties of galaxies seem to be almost independent of redshifts. This has already been described as "biased" galaxy formation, and Kauffmann et al. (1999b) have shown that the correlation length at which the two-point correlation function of galaxies becomes unity does not significantly evolve as dark matter does and that the bias of galaxy distribution to dark matter grows toward higher redshift. In a subsequent paper, we shall investigate clustering properties of galaxies in detail

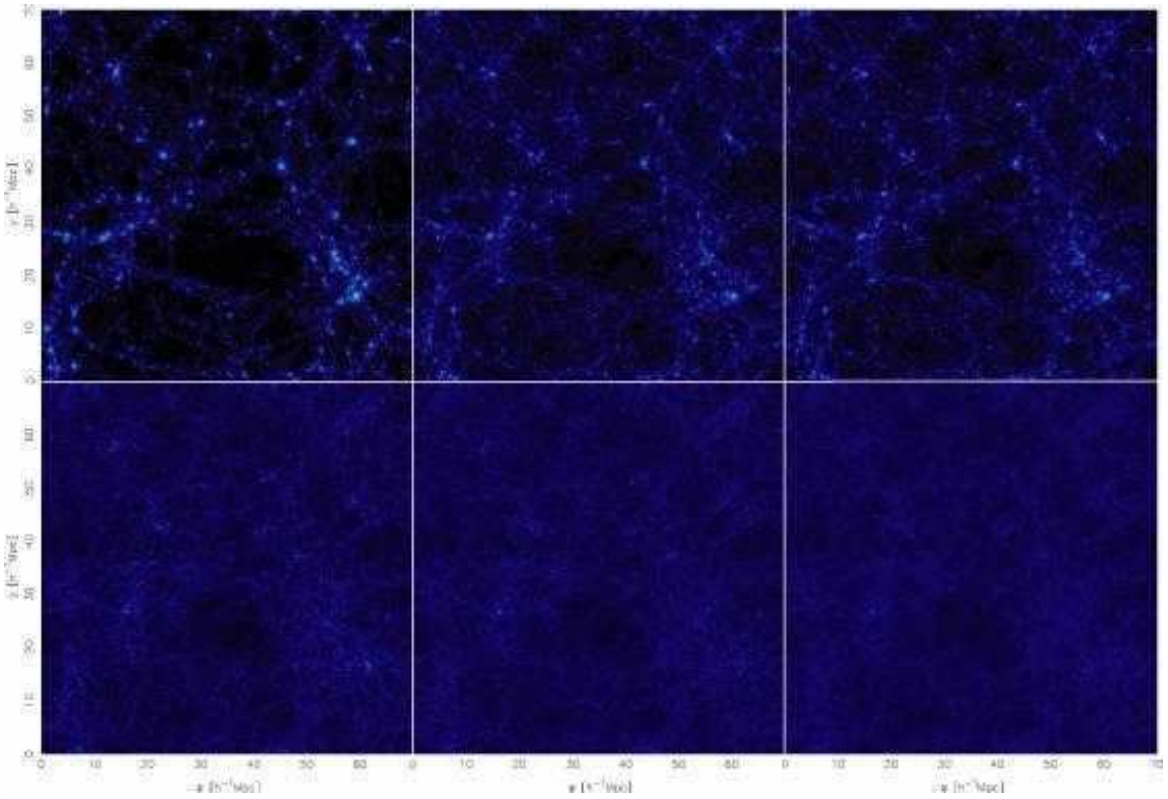

FIG. 5.— Projected distribution of dark matter in the $L = 70h^{-1}$ Mpc simulation at six redshifts: $z = 0$ (top left), 1 (top middle), 2 (top right), 3 (bottom left), 4 (bottom middle) and 5 (bottom right). Brighter regions indicate denser regions.

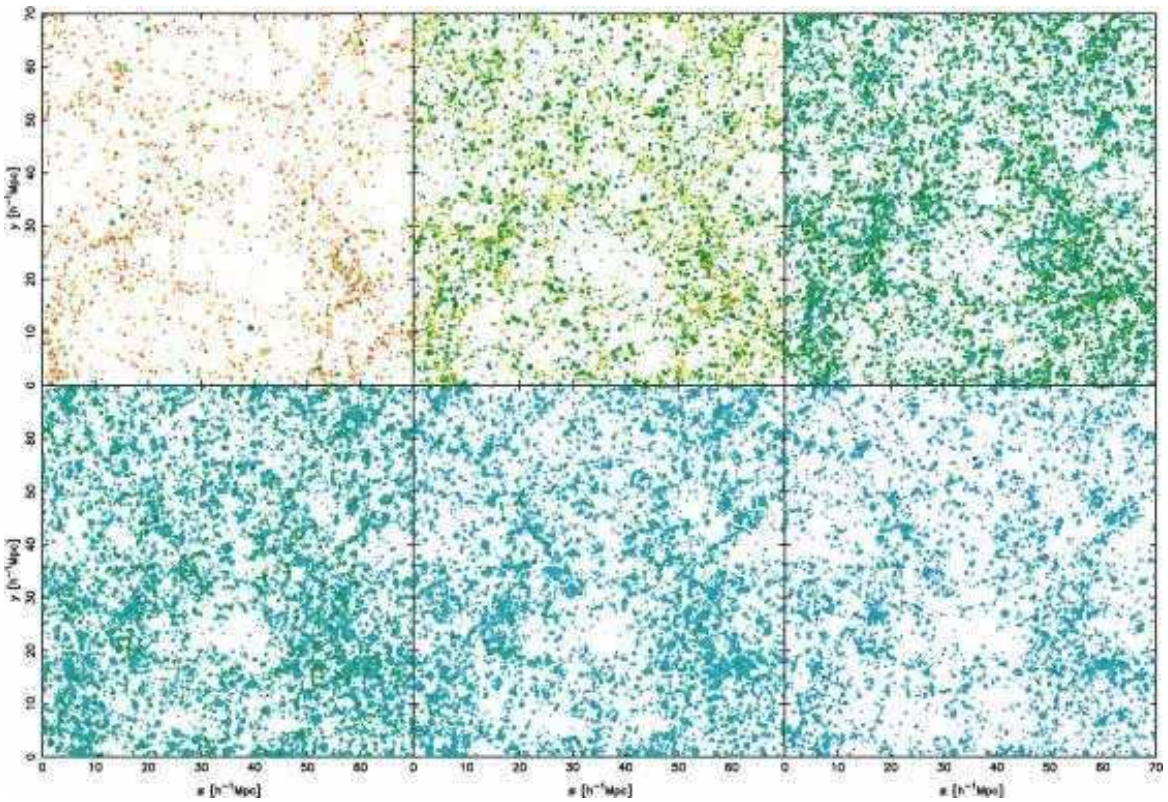

FIG. 6.— Same as Figure 5 but for galaxies. Plotted galaxies are $M_B \leq -19.5$ in their rest frames. Larger points represent brighter galaxies. Colors of points indicate the rest frame $B - V$ color of galaxies.

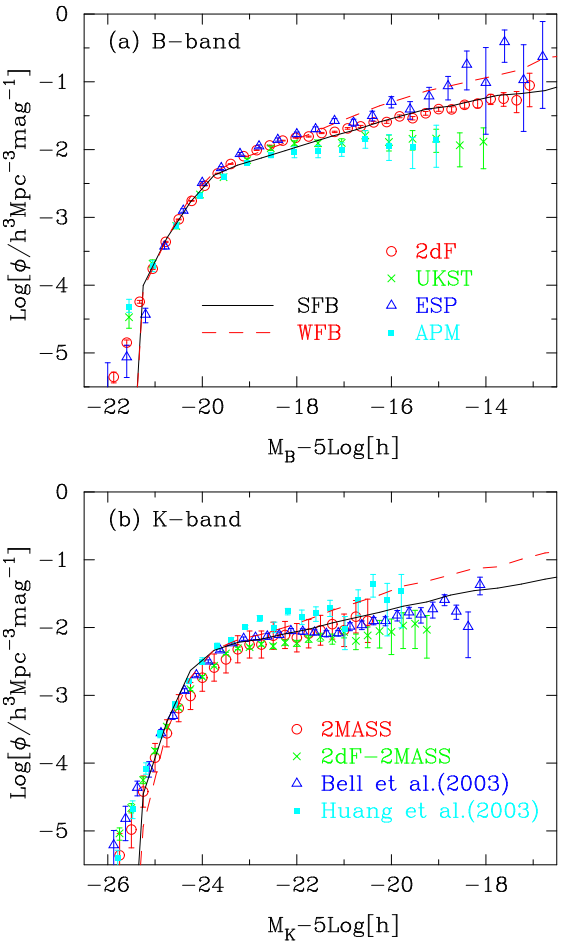

FIG. 7.— Local luminosity functions in the (a) B and (b) K bands. The solid and dashed lines represent the SFB and WFB models, respectively. Symbols with error bars in (a) indicate the observational data from APM (Loveday et al. 1992, *filled squares)*, ESP (Zucca et al. 1997, *open triangles)*, Durham/UKST (Ratcliffe et al. 1998, *crosses)*, and 2dF (Folkes et al. 1999, *open circles)*. Symbols in (b) indicate the data from 2MASS (Kochanek et al. 2001, *open circles)*, 2dF combined with 2MASS (Cole et al. 2001, *crosses)*, Bell et al. (2003, *open triangles)*, and Huang et al. (2003, *filled squares)*.

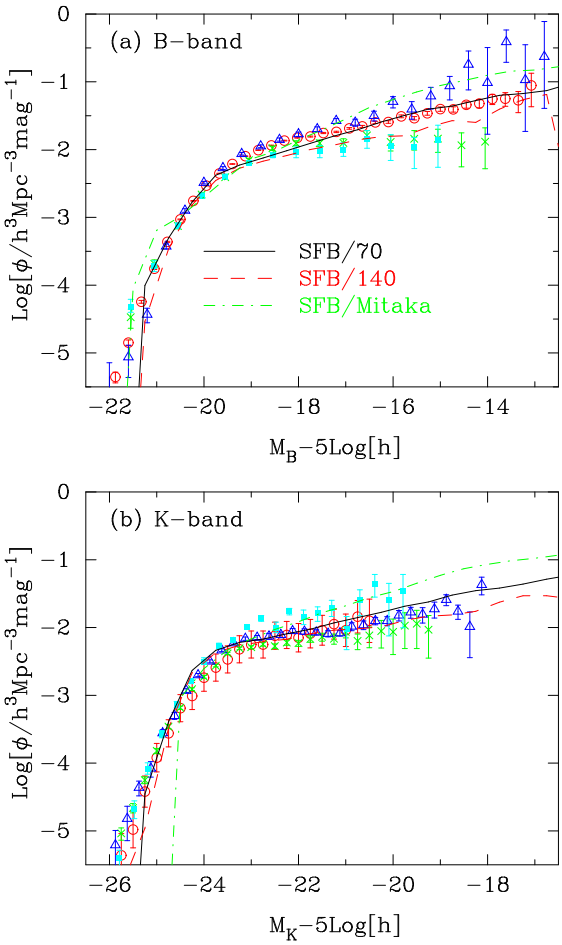

FIG. 8.— Local luminosity functions. Same as Figure 7, but for theoretical models plotted. The solid lines represent the same SFB model as shown in Figure 7, indicated by SFB/70 in (a). The dashed lines represent a model with the same parameters as the SFB model, but for the simulation box size of 140 h^{-1} Mpc, which has an eight times larger minimum mass of dark halos. The dot-dashed lines represent the Mitaka model given by NY04, but for the same parameters as the SFB model. The minimum mass of dark halos in this model is given by $V_{\rm circ} = 40$ km s^{-1}.

(Yahagi et al. 2005).

4. GALAXIES AT PRESENT

4.1. *luminosity functions*

Figure 7 shows B and K-band luminosity functions of galaxies. The solid and dashed lines represent the SFB and WFB models, respectively. Since the SF time-scale hardly affects local luminosity functions, they are determined almost solely by the SN feedback-related parameters, $\alpha_{\rm hot}$ and $V_{\rm hot}$. Symbols with error bars represent observational results from the B-band redshift surveys, such as Automatic Plate Machine (APM; Loveday et al. 1992), ESO Slice Project (ESP; Zucca et al. 1997), Durham/United Kingdom Schmidt Telescope (UKST; Ratcliffe et al. 1998) and Two-Degree Field (2dF; Folkes et al. 1999), and from the K-band redshift surveys given by Two Micron All Sky Survey (2MASS; Kochanek et al. 2001), 2dF combined with 2MASS (Cole et al. 2001), Bell et al. (2003) and Huang et al. (2003). The SFB model agrees well with the luminosity functions of 2dF and Bell et al. (2003), and the WFB model agrees with those of ESP and Huang et al. (2003).

It is interesting and important to assess the effects of numerical resolution on galaxies. This corresponds to the lower limit of the mass of dark halos. The N-body simulation we use is of a box size of 70 h^{-1} Mpc. Since all halos must have at least ten dark matter particles, the minimum mass M_{70} corresponds to $3.04\times10^9 M_\odot$. Here we use another result of an N-body simulation with a 140 h^{-1} Mpc box and the same number of dark matter particles. The minimum mass of halos is $M_{140} = 2.43\times10^{10} M_\odot = 8M_{70}$. The resultant luminosity functions for the 140 h^{-1} Mpc box simulation are shown in Figure 8 for the SFB model, indicated by the dashed lines (*SFB/140*), with the same astrophysical parameters as those of the 70 h^{-1} Mpc box simulation (*SFB/70; solid lines*). It is evident that this predicts fewer galaxies and a very shallow slope at the faint end. One of the reasons is clearly that the minimum mass of dark halos becomes larger. This is an effect similar to that resulting from the adoption of stronger SN feedback for low-mass halos so that hot gas cannot cool within dark halos below M_{140}. This means that if one would like to connect an obtained parameter set with physical processes such as the SN feedback, the numerical resolution would be crucial, while we should be able to construct a predictable model regarding those parameters as only phenomenological.

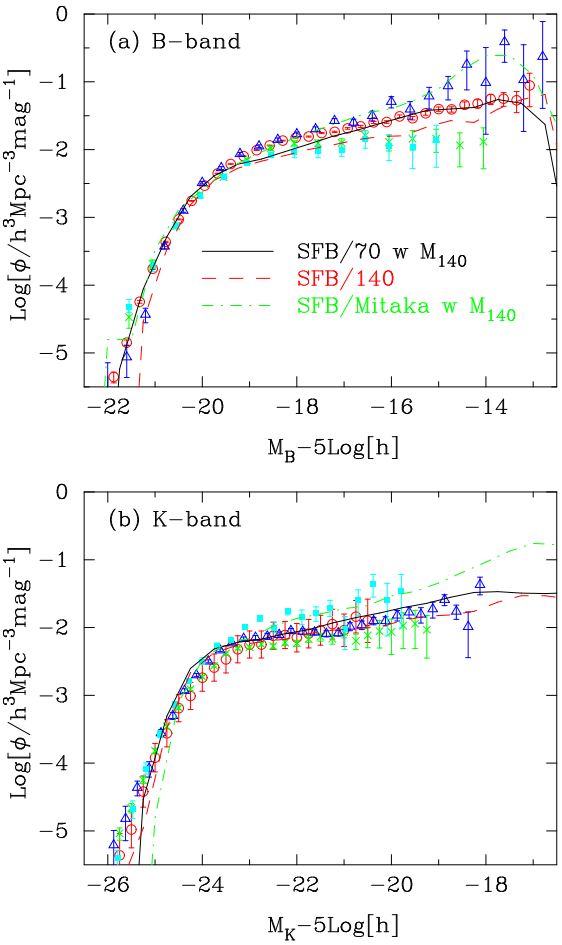

FIG. 9.— Local luminosity functions. Same as Figure 7, but for theoretical models. The solid lines represent the SFB model with the same minimum mass M_{140} as the SFB/140 model. Hot gas within halos between M_{70} and M_{140} do not cool at all. The dashed lines represent the same SFB/140 model as shown in Figure 8. The dot-dashed lines represent the Mitaka model with the minimum mass M_{140}.

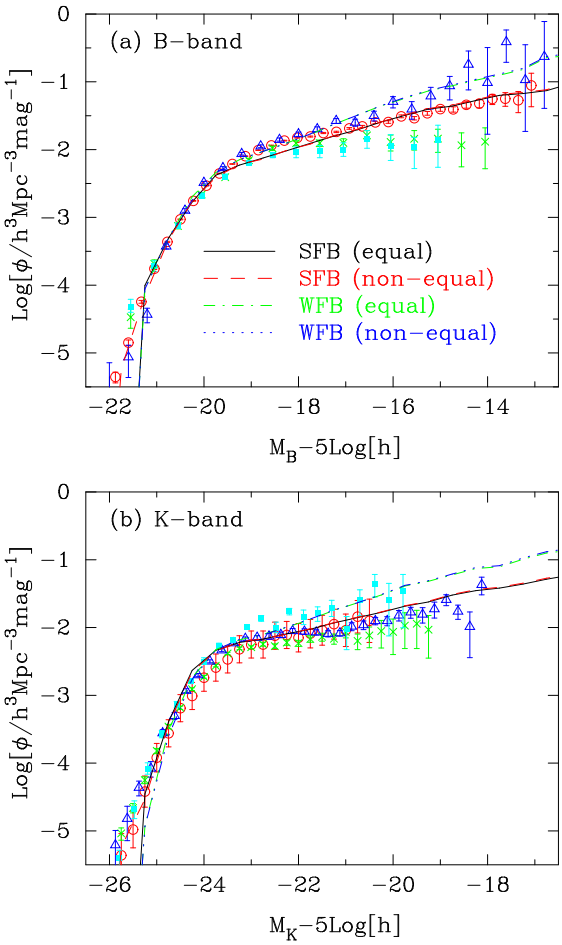

FIG. 10.— Local luminosity functions. Same as Figure 7, but for two added variant models. The solid and dot-dashed lines represent the SFB and WFB models, respectively, the same as those shown in Figure 7. The dashed and dotted lines also represent the SFB and WFB models, but including the effect of non-equal mass mergers between satellite galaxies described by eq.(27). Note that luminosity functions of models with and without the effect of non-equal mass mergers are almost identical.

Also plotted by the dot-dashed lines is the Mitaka model, but with the same parameters as those of the SFB model, which are slightly different from the original ones. In this model, the minimum mass of halos corresponds to $V_{\rm circ} = 40$ km s^{-1}. Part of the reason the faint-end slope is steeper than that of the SFB model should be that the minimum mass becomes smaller at high redshift when stars actively form. This is, however, only part of the reason. This is shown below. From this comparison, we would like to stress that we should denote attention to the minimum mass of dark halos, or the numerical resolution, which corresponds physically to the effective Jeans mass.

Further investigation of this problem provides interesting features. Figure 9 shows luminosity functions for the SFB and Mitaka models with the minimum mass M_{140} of halos indicated by the solid and dot-dashed lines, respectively, as well as the SFB/140 model by the dashed lines. At first, it is shown that the SFB/70 model with M_{140} does not recover the SFB/140 model, except for the cut-off at the faint end, $M_B - 5\log h \sim -14$. The change in the slope caused by the change in minimum mass is quite small. Therefore, the minimum mass seems to mainly affect only very faint galaxies. Second, the faint-end slope of the Mitaka model with M_{140} also hardly changes except for the cut-off. The bump at $M_B - 5\log(h) \simeq -14$ is a characteristic luminosity of the faintest galaxies determined by the higher minimum mass. In other words, galaxies formed in dark halos of the minimum mass without any progenitors should have such luminosities under the given strength of the SN feedback. Thus it is difficult for those to have fainter luminosities. This figure therefore shows again that the numerical resolution significantly affects galaxy formation, and that there is a limitation in the extended Press-Schechter formalism which gives us merging histories of dark halos.

We would like to stress here that this is *not* a convergence test. If the merger trees included less massive dark halos, the results would change further. In this case, the faint end of the luminosity function would become steeper because such small halos produce very faint galaxies. In our current model, although no realistic model of the effective Jeans mass is included, the mass resolution corresponding to M_{70} should be required for realistic modeling, because adopting M_{140} or larger minimum mass corresponds to overestimation of the effective Jeans mass. It should be very important to model the effective Jeans mass by utilizing higher-resolution simulations in future.

Finally, we discuss mergers of satellite galaxies. As shown

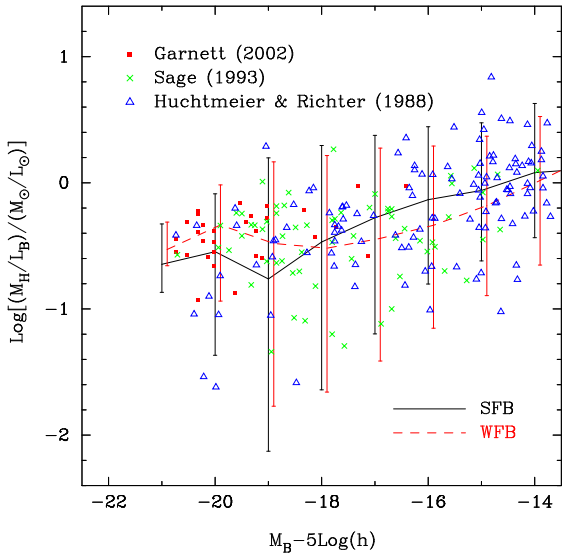

FIG. 11.— Hydrogen mass relative to B-band luminosity of spiral galaxies. The solid and dashed lines represent the medians for the SFB and WFB models, respectively, of the distributions of $M_{\rm H}/L_B$. The error bars indicate 25% and 75% percentile points. Symbols indicate the observational data from Huchtmeier & Richter (1988, *open triangles)*, Sage (1993, *crosses)*, and Garnett (2002, *solid squares)*. Note that the data from Huchtmeier & Richter (1988) include only H I.

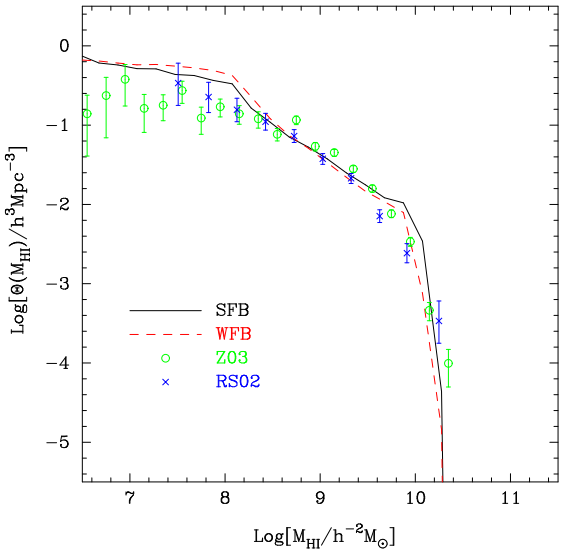

FIG. 12.— H I mass functions. The solid and dashed lines represent the SFB and WFB models, respectively. The crosses and open circles indicate the observational data from Rosenberg & Schneider (2002) and Zwaan et al. (2003), respectively. Again we set $M_{HI} = 0.75M_{\rm cold}$ for the theoretical models.

in eq.(27), our code enables us to take into account the effect of non-equal mass mergers between satellite galaxies based on Mamon (2000), while this is normally switched off. Figure 10 shows this effect on luminosity functions. The dashed and dotted lines indicate the SFB and WFB models with the effect of non-equal mass mergers, while the solid and dot-dashed lines indicate the SFB and WFB models without this effect, which are the same as those shown in Figure 7. It is easily seen that the luminosity functions with and without the effect of non-equal mergers are almost identical except for the bright end. Therefore, we conclude that, fortunately, we do not need to consider the effect of non-equal mass mergers. Thus we consider only equal mass mergers using the rate of $k_{\rm MH}$ given by Makino & Hut (1997) below.

4.2. *cold gas*

The amount of cold gas, which corresponds to the interstellar medium, is mainly determined by SN feedback-related and SFR-related parameters. The former parameters determine the gas fraction expelled from galaxies, and the latter, the gas fraction that is converted into stars. Because the SN feedback-related parameters are already constrained by matching luminosity functions as shown in the previous subsection, we can use observed gas fractions in spiral galaxies as constraints on the SFR-related parameters, α_* and τ_*^0.

Figure 11 shows the ratio of cold gas mass relative to B-band luminosity of spiral galaxies as a function of their luminosity. We assume here that 75% of the cold gas in the models is comprised of hydrogen, i.e., $M_{\rm H} = 0.75M_{\rm cold}$. The solid and dashed lines associated with error bars represent the medians and 25% and 75% percentiles of the distributions for the SFB and WFB models, respectively. We have added 0.1 mag offsets to the data of the WFB model for error bars to be distinguishable. Symbols indicate the observational data of individual galaxies taken from Huchtmeier & Richter (1988, *open triangles)*, Sage (1993, *crosses)*, and Garnett (2002, *solid squares)*. Note that the data from Huchtmeier & Richter (1988) include only H I, and that the fraction of hydrogen molecule, H_2, usually increases with the luminosity. Although the medians for both models are in good agreement with the observations, the error bars for the theoretical models seem to be larger than the distribution of the observational data. This might suggest the existence of self-regularization mechanisms of star formation to develop small scatters of cold gas fraction. Nevertheless, we can say that the models agree well with the observational data.

Adopted values of the parameters for the SF model are tabulated in Table 3. The SFB model has $\alpha_* = -4$, which means $\tau_* \propto \beta$. This is similar to the prescription of the SF timescale in NY04, $\tau_* \propto (1+\beta)$. On the other hand, in the WFB model, we have to set $\alpha_* = -2.3 \neq -\alpha_{\rm hot}$. Unfortunately, the simple prescription of NY04 does not work for weak SN feedback models.

Recent radio surveys have provided good data of H I mass functions (HIMFs). Figure 12 shows the theoretical prediction of HIMFs for the SFB and WFB models, respectively. Both models provide almost identical HIMFs, because we have chosen the SFR-related parameters to be consistent with the observed cold gas fractions. Symbols indicate the observational data from Rosenberg & Schneider (2002, *crosses)* and Zwaan et al. (2003, *open circles)*. Both models reproduce the observed HIMFs quite well. Note that we again assume $M_{\rm HI} = 0.75M_{\rm cold}$.

4.3. *galaxy sizes*

Figure 13 shows the effective disk radii of local spiral galaxies as a function of their luminosities. The solid and dashed lines represent the SFB and WFB models, respectively. Symbols are the observational data taken from Impey et al. (1996). To avoid confusion, we have added 0.1 mag offsets to the WFB model. Here we would like to briefly repeat the procedure to determine the disk size. Dark halos form with angular momenta randomly assigned with the log-normal distribution of the dimensionless spin parameter, $\lambda_{\rm H}$

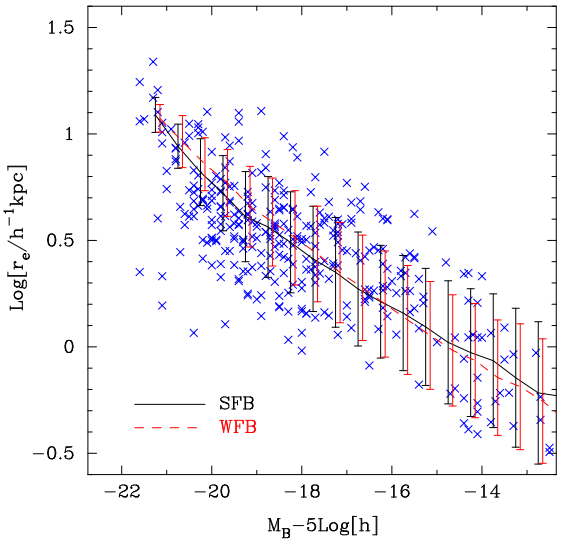

FIG. 13.— Disk size of spiral galaxies. The solid and dashed lines represent the averages of disk radii of spiral galaxies in the SFB and WFB models, respectively. Error bars on these lines are 1 σ scatter in predicted sizes. To avoid any confusion, 0.1 mag offsets are imposed on the results of the WFB model. Crosses indicate the observational data taken from Impey et al. (1996).

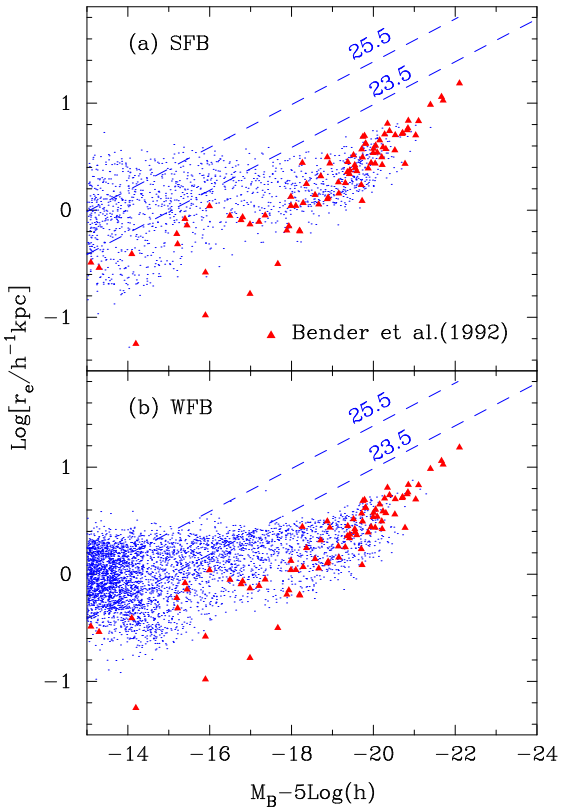

FIG. 14.— Sizes of elliptical galaxies. The dots represent effective radii of individual elliptical galaxies in (a) the SFB model and (b) the WFB model. Only a quarter of all elliptical galaxies is plotted. The filled triangles indicate the observational data taken from Bender, Burstein & Faber (1992). The dashed lines denote constant surface brightnesses, 23.5 and 25.5 mag arcsec^{-2}, as indicated in panels.

(eq. 28). Hot gas contained in a dark halo is assumed to have the same specific angular momentum as that of the halo. The hot gas cools and contracts until the cooled gas is rotationally supported. Thereby the size of disks is determined. Good agreement of the theoretical models with the observational data shown in this figure means that the standard assumption we adopt for determining disk sizes works well when the distribution of the dimensionless spin parameter is in a reasonable range, estimated from the structure formation theory in the CDM universe.

Correctly estimating disk sizes is very important to compare theoretical models with observations because it affects many observational properties of galaxies such as the surface brightness and the dust column density. Nagashima et al. (2001, 2002) have discussed such effects caused by the uncertainty in estimating disk sizes.

Figure 14 shows the effective radii of elliptical galaxies against their B-band magnitudes. The dots represent individual elliptical galaxies in the (a) SFB and (b) WFB models. The effective radius r_e is estimated from $r_e = 0.744 r_b$ (Nagashima & Yoshii 2003), where r_b is the three-dimensional half-mass radius [eqs.(33) and (34)]. To make figures clearer, only a quarter of all ellipticals are plotted. The solid triangles indicate the observational data taken from Bender, Burstein & Faber (1992). The theoretical models agree well with the observational data of at least brighter than $M_B - 5\log(h) \simeq -18$. At magnitudes fainter than that, the fraction of compact ellipticals in the models seems to be smaller than that expected from the observations. This would be partly caused by the limited resolution. Another possibility is that the SF time-scale at high redshift might be slightly too long. As clearly shown by NY04, the size of dwarf ellipticals strongly depends on the SF time-scale at high redshift. For example, let us consider the SF time-scale simply proportional to the dynamical time-scale. In this case, the SF time-scale is shortened for higher redshift, and at $z = 2$, it becomes nearly a quarter of that at $z = 0$. Noting that the SF time-scale also determines the rate of gas consumption, therefore, galaxies are statistically gas-poorer than those in the case of the constant SF time-scale over all redshifts at high redshift, at which galaxies frequently merge. Evidently, because the change in size and velocity dispersion due to the dynamical response becomes smaller, galaxies with small sizes and large velocity dispersions increase. As shown by NY04, some compact ellipticals represented in Figure 14 are closely related to ellipticals formed via gas-poor mergers. Although we are able to make such compact ellipticals by slightly shortening the SF time-scale at high redshift with an extra parameter relating to the redshift dependence, we would like to leave it constant to avoid further complexity of the model. A detailed discussion about the relationship between the SF time-scale and the size and velocity dispersion of ellipticals can be found in NY04.

The dashed lines represent constant surface brightnesses of 23.5 and 25.5 mag arcsec^{-2} as indicated in the figure. Because the detection of galaxies is limited by the surface brightness, galaxies with surface brightness lower than the detection limit, which depends on observations, cannot be detected. Although our models apparently predict too many dwarf ellipticals with radii larger than about 1 h^{-1} kpc, they will not be observed unless ultra deep observations are performed. Note that the samples of galaxies from Bender, Burstein & Faber (1992) may be expected to have sufficiently high surface brightness to investigate their structural and kinematical properties, because the purpose of the paper is to clarify those properties. Thus it should not be a problem that many dwarf ellipticals with much larger radii emerge. In fact, the selection

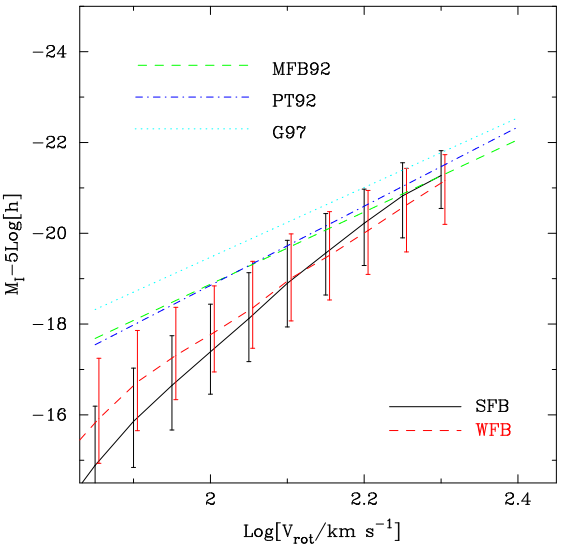

FIG. 15.— I-band Tully-Fisher relation of spiral galaxies. The solid and dashed lines associated with error bars indicate the medians and 25% and 75% points of the distributions of I-band magnitudes for the SFB and WFB models, respectively. To avoid confusion, 0.1 mag offsets are imposed on the results of the WFB model. The observed TF relations are shown as a mean relation given by Mathewson, Ford & Buchhorn (1992, *thin dashed line)*, Pierce & Tully (1992, *thin dot-dashed line)*, and Giovanelli et al. (1997, *thin dotted line)*.

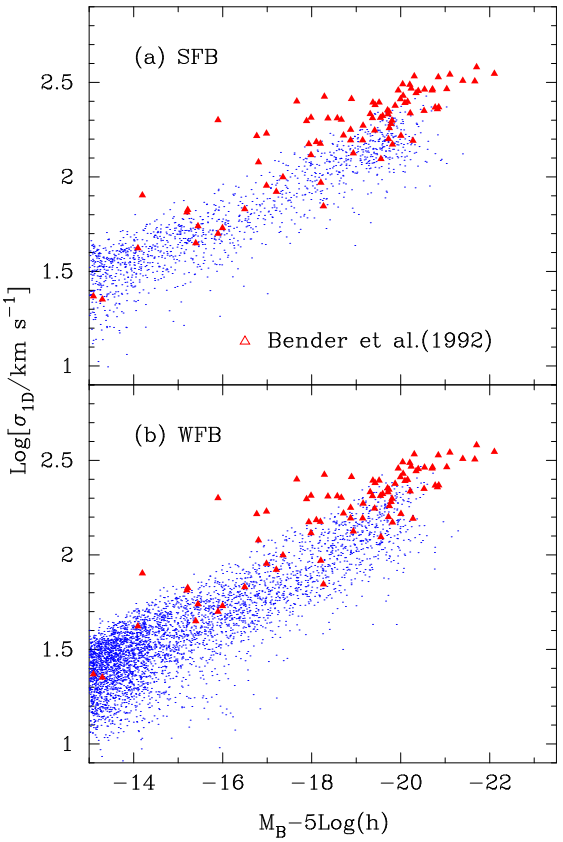

FIG. 16.— B-band Faber-Jackson relation of elliptical galaxies. The dots represent one-dimensional velocity dispersions of individual elliptical galaxies in (a) the SFB model and (b) the WFB model. Only a quarter of all elliptical galaxies is plotted. The filled triangles indicate the observational data taken from Bender, Burstein & Faber (1992). The velocity dispersion of the models is simply estimated as $\sigma_{1D} = V_b/\sqrt{3}$.

effects brought about by the surface brightness play a significant role for high redshift galaxies. This will be shown in §5.

4.4. *velocity-magnitude relations*

Here we investigate velocity-magnitude relations, that is, the Tully-Fisher (TF) relation for spiral galaxies (Tully & Fisher 1977) and the Faber-Jackson (FB) relation for elliptical galaxies (Faber & Jackson 1976).

Figure 15 shows the I-band TF relation. The solid and dashed lines associated with error bars represent the medians and 25% and 75% points of the distributions of I-band magnitudes for the SFB and WFB models, respectively. While gas-rich spirals tend to be more luminous as indicated by Cole et al. (2000) and NY04, we show only the results for all spiral galaxies. We find that, although not shown, the TF relation produced only by gas-rich spirals becomes too bright, particularly at $V_{\rm rot} \sim 130$ km s^{-1} and too steep at $V_{\rm rot} \lesssim 100$ km s^{-1} to reconcile with observations in both models. The straight lines indicate the results best fit to the observed TF relations of Mathewson, Ford & Buchhorn (1992, *dashed)*, Pierce & Tully (1992, *dot-dashed)*, and Giovanelli et al. (1997, *dotted)*. We assume that the linewidth W is simply twice the disk rotation velocity, $V_{\rm rot}$, as usual. For model galaxies, we set $V_{\rm rot} = V_d$.

At faster than $V_{\rm rot} \simeq 160$ km s^{-1} [$\log(V_{\rm rot}/{\rm km\,s^{-1}}) \simeq 2.2$], both the theoretical models agree well with the observational TF relations. Besides, the WFB model is marginally consistent with some of the observations down to $V_{\rm rot} \simeq 100$ km s^{-1}, while the TF relation of the SFB model deviates and has a steeper slope compared with the observations. As shown in NY04, the slope is mainly determined by $\alpha_{\rm hot}$ because it provides the dependence of the strength of the SN feedback on the velocity and therefore affects luminosities, particularly of dwarf galaxies. The deviation at small velocities might disappear if the dynamical response on the rotation velocity to gas removal due to the SN feedback is taken into account, which is currently applied only to spheroidal formation by starbursts. Because dwarf galaxies significantly suffer from the SN feedback, disks may expand and rotate slowly.

Figure 16 shows the B-band FJ relation of elliptical galaxies. The dots represent individual ellipticals in the (a) SFB and (b) WFB models. The model predictions broadly agree with the observational data from Bender, Burstein & Faber (1992). This agreement is obtained thanks to $f_{\rm diss} = 1.3$. In the case of $f_{\rm diss} = 1$ as in NY04, the models predict smaller velocity dispersions than the observations. The reason $f_{\rm diss} = 1.3$ is required in this model would be the differences of the SN feedback and the SF time-scale. Dwarf galaxies with $\sigma_{1D} \lesssim 20$ km s^{-1} can be obtained only by associating with the dynamical response (see Figure 2) as shown by NY04, in which the effect of the dynamical response was introduced into SA models for the first time. Detailed discussion on the velocity dispersion of dwarf galaxies can be found in the previous subsection and NY04.

4.5. *color-magnitude relations*

Figure 17 shows the $V - K$ color-magnitude (CM) diagram for cluster elliptical galaxies. Cluster halos that we pick out have masses of 6.18, 4.07, 2.99, 2.71, and 2.68 $\times 10^{14} M_\odot$, which are five of the most massive halos in our simulation. Different symbols represent elliptical galaxies in different clusters. The solid line indicates a CM relation

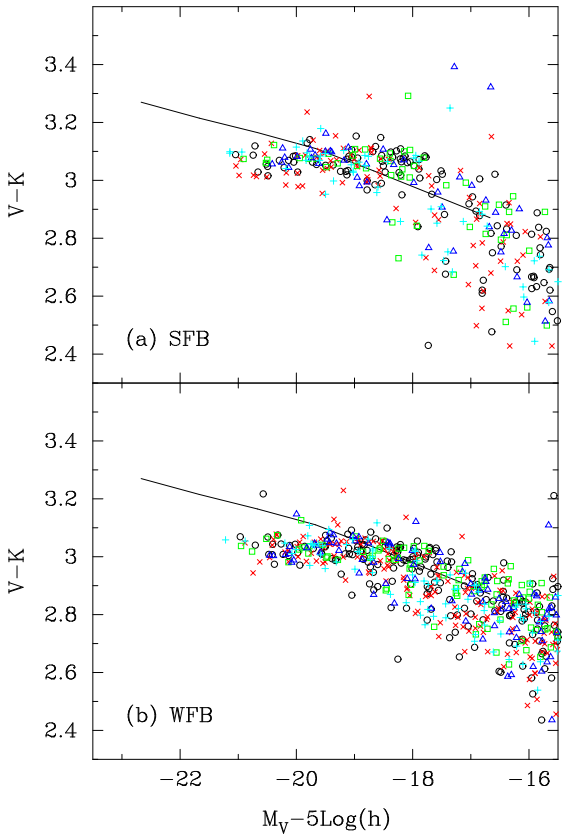

FIG. 17.— $V-K$ color-magnitude relations of elliptical galaxies in five of the most massive clusters in the (a) SFB and (b) WFB models. Different symbols represent ellipticals in different clusters. The solid line is the observed CM relation of the Coma cluster with a correction to the aperture effect by Kodama et al. (1998)

provided by Kodama et al. (1998), which is corrected for the aperture effect on the observational CM relation for the Coma cluster obtained by Bower, Lucey & Ellis (1992). While the models agree with the observation for dwarf ellipticals, $M_V - 5\log(h) \gtrsim -18$, the predicted CM relations become almost flat for giant ellipticals. This trend is similar to previous work on SA models whose model parameters are chosen so that many other observations such as luminosity functions are reproduced (Cole et al. 2000; Nagashima & Yoshii 2004). The mechanism itself to make the slope of the CM relation is well understood in terms of the SN feedback. The slope for dwarf ellipticals is mainly determined by $\alpha_{\rm hot}$ and the break point at which the CM relation becomes flat mainly by $V_{\rm hot}$ (Kauffmann & Charlot 1998; Nagashima & Gouda 2001).

To improve this situation, the metal enrichment should be much more carefully considered because the CM relation mainly follows the metallicity-luminosity relation (Kodama & Arimoto 1997; Kauffmann & Charlot 1998; Nagashima & Gouda 2001). In this paper, the chemical yield is set at twice the solar value (e.g. Kauffmann & Charlot 1998; Somerville & Primack 1999). This is required to obtain colors of cluster ellipticals similar to observations. However, this value is too large compared with yields derived from standard IMFs for disk star formation such as Salpeter's, which provide almost solar values. Moreover, a recent SA analysis by Nagashima & Okamoto (2004) has shown that a Salpeter-like IMF successfully reproduces observed stellar distributions on an [O/Fe]-[Fe/H] plane. A possible solution is to adopt different IMFs for different modes of star formation. Baugh et al. (2005) and Nagashima et al. (2005a) have suggested Kennicutt's IMF for disk star formation and a top-heavy IMF for starbursts. Although this should be worth considering, it is beyond the scope of this paper at this stage of our modeling.

5. HIGH REDSHIFT GALAXIES

5.1. *Faint Galaxy Number Counts*

Counting galaxies in a unit area is a task fundamental to observations in astrophysics (e.g., Yoshii & Takahara 1988). It also provides important constraints on galaxy formation theories as shown in Nagashima et al. (2001, 2002). Figure 18 shows faint galaxy number counts in the optical $BVRi'z'$-bands. Symbols indicate observed counts taken from Kashikawa et al. (2004), obtained by the *Subaru Deep Survey* (SDS) using the Suprime-Cam with a substantially large field-of-view, $34' \times 27'$, so the data are very reliable in a statistical sense, compared with observations by other telescopes such as the *Hubble Space Telescope* (HST). In this figure, we add offsets to magnitudes depending on pass-bands to avoid confusion. Note that these data are observationally *raw*, which means that no correction to selection effects is considered and that the isophotal AB magnitude is used. The solid and dashed lines represent the SFB and WFB models, respectively. The thick and thin lines denote models with and without selection effects arising from cosmological dimming of surface brightness (Yoshii 1993). To estimate the selection effects, we need detection limits of surface brightness dependent on observations and on seeing of observations which determines the FWHM of images. The details of the selection effects are shown in Totani & Yoshii (2000), and in Nagashima et al. (2001) within the framework of SA models. In these optical pass-bands, as shown in Figure 18, both models agree incredibly well with the observed galaxy counts when the selection effects are included. We have confirmed that these models also reproduce galaxy counts well in the Hubble Deep Field (HDF), as shown for the Mitaka model in NY04. Note that models of dust optical depth for the SFB and WFB models are different at high redshift as shown in eq.(38). We adopt $\rho = 1$ for the SFB model and $\rho = 0$ for the WFB model, which means that the dust extinction at high redshift in the WFB model is stronger than in the SFB model. If we adopted $\rho = 0$ for the SFB model, it would underestimate the number of faint galaxies because of the strong dust extinction.

Figure 19 shows galaxy counts in the near-infrared K'-band. Open circles associated with error bars indicate observed counts in the *Subaru Deep Field* (SDF) taken from Maihara et al. (2001). We should warn readers that the field-of-view for the near-infrared SDF is only $2' \times 2'$, which is less than 1% of the area for the optical SDF. Other symbols are ground-based observed counts from Glazebrook et al. (1994, *open stars)*, Minezaki et al. (1998, *filled squares)*, McLeod et al. (1995, *filled triangles)*, and Gardner et al. (1996, *filled circles)*. The plotted data are also raw counts. The lines denote the same meanings as those in Figure 18. For K'-band counts, moreover, the completeness arising from noise and statistical fluctuations is also taken into account. The details are shown in Totani et al. (2001) and Nagashima et al. (2002). Different from the optical counts shown in Figure 18, the agreement with the observations is worse for both models, which overestimate the number of galaxies at $K' \sim 23$. The SFB model provides somewhat

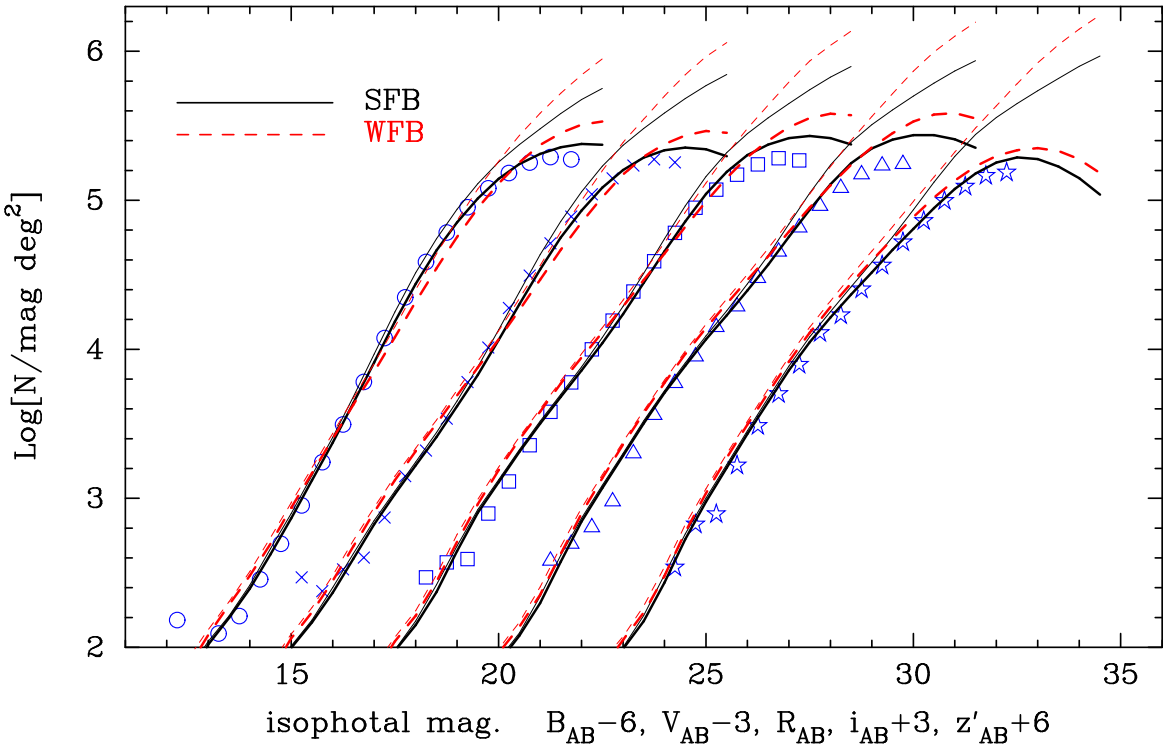

FIG. 18.— Galaxy number counts in the $BVRi'z'$ bands from the left to the right. To avoid any confusion, offsets of -6, -3, +3, and +6 magnitudes are added for B, V, i', and z' bands, respectively. The solid and dashed lines represent the SFB and WFB models, respectively. The thick and thin lines denote models with and without the selection effects, respectively, arising from the same detection threshold of surface brightness of galaxies as employed in the SDS. Symbols indicate the observed SDS counts.

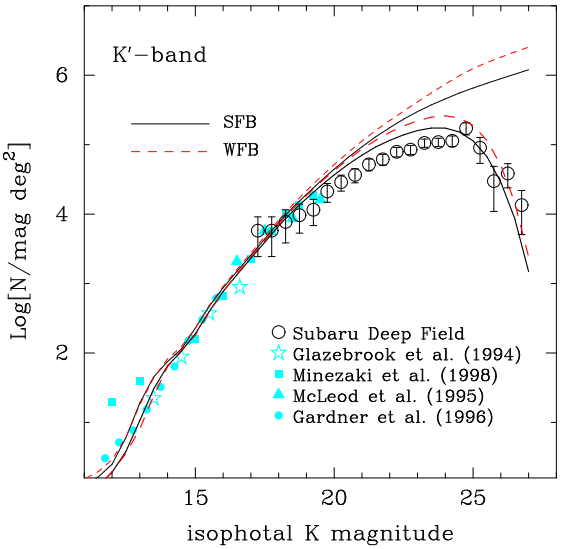

FIG. 19.— Galaxy number counts in the K' band. Same as Figure 18, but for the near-infrared counts in the SDF. Open circles associated with error bars indicate the observed SDF counts from Maihara et al. (2001). Other symbols are ground-based observed counts as indicated in the figure.

better agreement than the WFB model. This is because, in the WFB model, more galaxies are formed at high redshift than in the SFB model, due to the weakness of the SN feedback. Note that the K' band magnitude mainly reflects the stellar mass of galaxies, while optical pass-bands magnitudes reflect the SFR. Because the K' band magnitude is not significantly affected by dust extinction compared with optical bands, one might consider that a possible way for the WFB model to recover the observed near-infrared counts should be stronger selection effects. However, such a manipulation also affects the optical galaxy counts, which are already reproduced. Thus, in the range of current modeling, we prefer the SFB model to the WFB, from the K' band galaxy counts.

Finally, we should recall that the above results are due to the choice of the redshift dependences of the size and optical depth, ρ and γ. In order to obtain the reasonable agreement shown here, it is necessary to introduce these parameters into simple models of estimating the disk size and the dust optical depth. Although it is quite difficult at this stage to derive the values physically, they will provide important keys to understanding of the physics of galaxy formation at high redshift.

5.2. *Redshift distributions*

Figure 20 shows I_{814} band photometric redshift distribution for the HDF galaxies. From the top to the bottom, galaxies for the bright-magnitude bin to the faint-magnitude bin are shown. The solid and dashed lines represent the SFB and WFB models, respectively. The thick and thin lines denote models with and without the selection effects, which are estimated from the same detection criteria as those for the HDF. The histograms are the observed photometric redshift distribution taken from Furusawa et al. (2000). In the brightest bin (panel *a*), both models agree well with the observation. The SFB model also agrees with the observation over all bins. However, as magnitudes of galaxies go fainter, the deviation from the observation for the WFB model increases. Although the peak of the distribution of galaxies above the surface brightness threshold for the HDF is similar to the observation, too many galaxies are detected in the WFB model

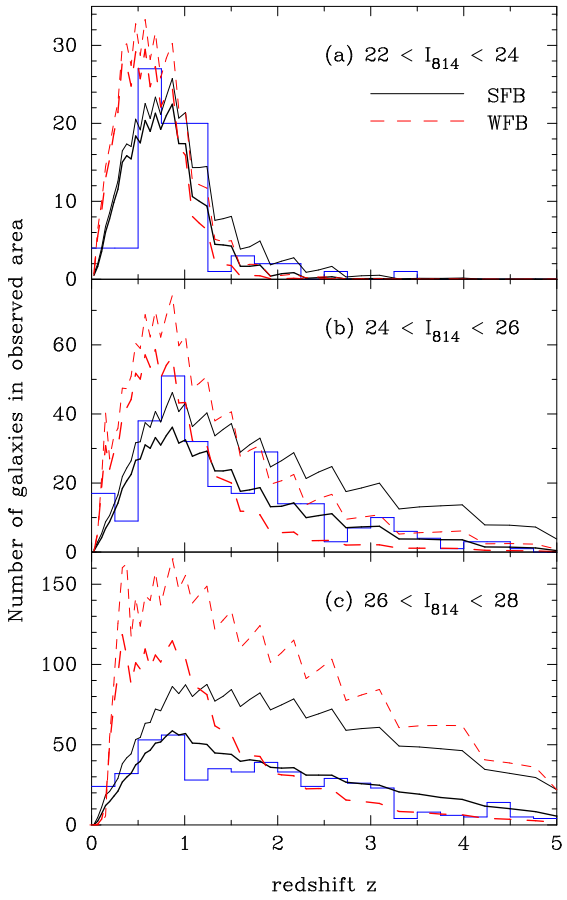

FIG. 20.— Redshift distribution of the HDF galaxies for (a) $22 < I_{814} \leq 24$, (b) $24 < I_{814} \leq 26$, and (c) $26 < I_{814} \leq 28$. The solid and dashed lines represent the SFB and WFB models, respectively. The thick and thin lines denote models with and without the selection effects, respectively. The histogram in each panel is the observed photometric redshift distribution by Furusawa et al. (2000).

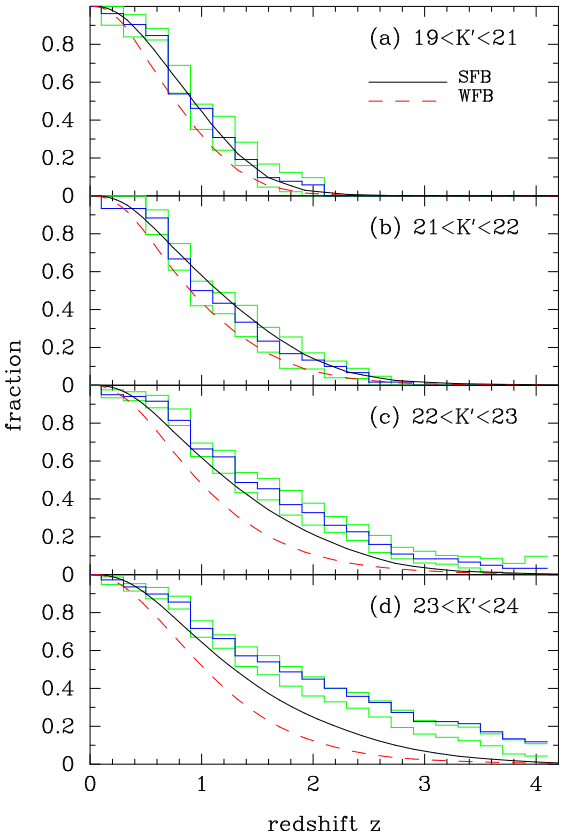

FIG. 21.— Normalized cumulative redshift distribution for the SDF galaxies for (a) $19 < K' \leq 21$, (b) $21 < K' \leq 22$, (c) $22 < K' \leq 23$, and (d) $23 < K' \leq 24$. The solid and dashed curves represent the SFB and WFB models, respectively. The histograms shown by the solid lines indicate the observed redshift distribution. Those indicated by the thin lines show the $\pm 3\sigma$ deviated counts estimated by Monte Carlo realizations when photometric redshift errors are taken into account [see Kashikawa et al. (2003) for details].

to be consistent with the observation. The weak SN feedback is obviously in part responsible for this deviation, because it cannot suppress the formation of dwarf galaxies at low redshift. Another important reason is the selection effects. As shown by the thin lines, the number of galaxies including undetectable ones is comparable (panel *b*) or sufficiently large (panel *c*) compared with the observation. However, since the selection effects are quite strong, only a small fraction of galaxies at high redshift can satisfy the detection criteria for the HDF. Therefore, the number of detectable galaxies for the WFB model is smaller than that for the SFB model at high redshift. Of course, it is possible to increase the number of detectable galaxies at high redshift by changing the detection criteria and/or by changing the redshift dependence of disk sizes. In this case, however, too many faint galaxies would emerge to reconcile with the number of galaxies at low redshift and with the observed galaxy number counts. It is evident that suppression of galaxy formation is necessary only at low redshift in order to match the redshift distribution for the WFB model with the observation. Thus, unless such mechanisms are found, the WFB model is inconsistent with the observation.

Figure 21 shows K' band normalized cumulative redshift distribution for the SDF galaxies. The solid and dashed lines represent the SFB and WFB models, respectively. Only models with the selection effects are plotted. The histograms indicated by the solid lines are the observed redshift distribution taken from Kashikawa et al. (2003). Those indicated by the thin lines show the $\pm 3\sigma$ deviated counts estimated by Monte Carlo realizations when photometric redshift errors are taken into account. The SFB model agrees significantly well with the observation in the top two panels *a* and *b*, which shows galaxies in the two brightest bins. In panel *c*, the agreement is only marginal. Although in panel *d*, the deviation from the observation is large, we should note quite large errors in estimating photometric redshift in this magnitude range, as shown in Figure 2 of Kashikawa et al. (2003). On the other hand, the difference between the WFB model and the observation is large for faint galaxies, $K' > 22$ (panels *c* and *d*). The main epoch of galaxy formation in the WFB model is at lower redshift than that in the SFB model, as shown in Figure 20.

In Kashikawa et al. (2003), the observational data were compared with an old version of the Mitaka model given by Nagashima et al. (2002). In that model, parameters are similar to those of the SFB model, rather than those of the WFB model. Nevertheless, the behavior of the old Mitaka model is very similar to that of the WFB model. We have confirmed that the Mitaka model presented in NY04 also shows a tendency similar to the WFB model. The reason the redshift distribution for the SFB model is improved should be the adop-

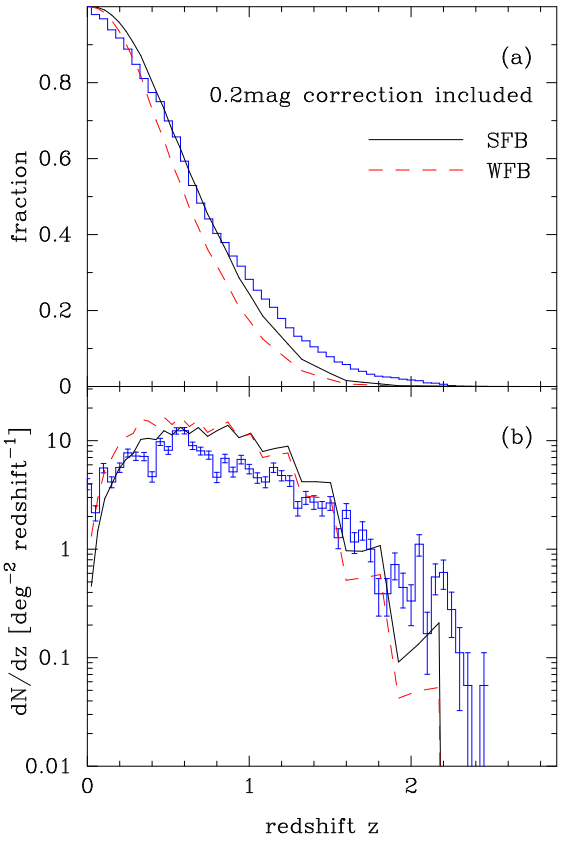

FIG. 22.— (a) Normalized cumulative redshift distribution for the GOODS $K_{AB} < 22$ galaxies. (b) Same as panel *a* but for the differential redshift distribution. The solid and dashed lines represent the SFB and WFB models, respectively. The histograms are the observed redshift distribution. Error bars in panel *b* denote 1 σ Poisson scatter. To obtain the isophotal magnitude used in the GOODS observations, a correction of 0.2 mag is applied to the models according to Somerville et al. (2004).

tion of merging histories of dark halos directly taken from N-body simulations. This might suggest that using correct merging histories is crucial to understanding of high redshift galaxies.

Finally, we compare our models with recent, larger samples from the Great Observatories Origins Deep Survey (GOODS) data. Figure 22 shows the (a) normalized cumulative redshift distribution and (b) differential redshift distribution for the GOODS galaxies of $K_{AB}(= K_{\rm Vega} + 1.85) < 22$. The solid and dashed curves represent the SFB and WFB models, respectively. The histograms are the observed GOODS redshift distribution from Somerville et al. (2004). Error bars in panel *b* denote 1 σ Poisson scatter. To obtain the isophotal magnitude, according to their paper, we make all galaxies 0.2 mag fainter than their total magnitudes. The SFB model seems to provide redshift distribution similar to their SA model shown in their Figure 1. Although the SFB model a little overestimates the number of galaxies at $z \sim 1$, the predicted number of those galaxies at $z \gtrsim 1.5$ seems slightly closer to the observation than their SA model. In the WFB model, similar to the previous figures on redshift distribution, the agreement with the observation is worse compared with the SFB model and the fraction of low redshift galaxies becomes larger. This is also because of the weakness of the SN feedback. Thus, we can also say that the SFB model is more consistent with the GOODS redshift distribution than the WFB model.

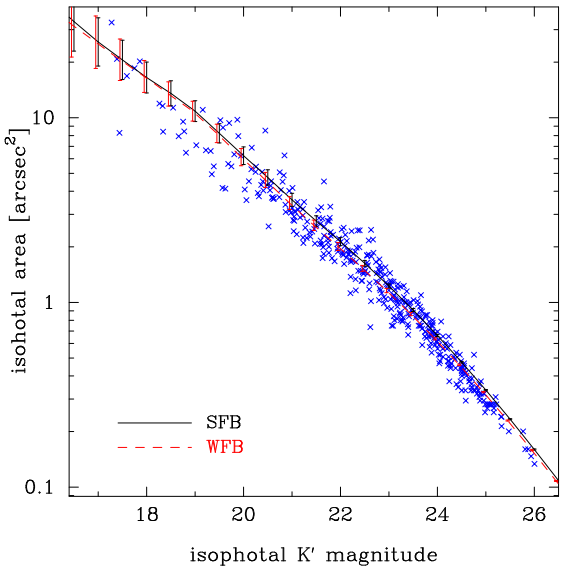

FIG. 23.— Isophotal area of the SDF galaxies against K'-magnitude. The solid and dashed lines associated with error bars of 1 σ scatter represent the SFB and WFB models, respectively. To avoid confusion, small offsets are added to the magnitude of the WFB model. The isophoto is calculated from the observational condition employed in the SDF survey. The crosses indicate the observational data from the SDF survey.

In short, the SFB model is consistent with the photometric redshift distribution for $I_{814} < 28$ and $K' < 23$ and the WFB only for $I_{814} < 24$ and $K' < 22$. Currently, observational data are still limited in number and in accuracy of estimation of redshift, particularly for near-infrared pass-bands. Wider and deeper surveys in future with accurate determination of redshifts, will provide better constraints on galaxy formation.

5.3. *Angular sizes*

Figure 23 shows the isophotal area of galaxies plotted against their K'-magnitude. The solid and dashed lines associated with error bars of 1 σ scatter represent the SFB and WFB models, respectively. To avoid confusion, small offsets are added to the magnitude of the WFB model. To obtain the isophoto, the same observational condition employed in the SDF survey is used. The crosses indicate the observational data from the SDF survey. This good agreement with the observations means that the models correctly estimate not only the size of galaxies, but the selection effects arising from the cosmological dimming of surface brightness of galaxies.

5.4. *Colors*

The evolution of colors of galaxies depends on growth of stellar mass, stellar ages, and dust extinction. Thus we are able to extract a great deal of information from galactic colors.

Figure 24 shows $R - K$ colors of galaxies in the AB system against their redshift. Because of comparison with the GOODS galaxies, we also adopt the selection criterion $K_{AB} + 0.2 < 22$, where we add 0.2 mag to our models to obtain the isophotal magnitude. In panel *a*, the GOODS galaxies, retrieved from Figure 2 of Somerville et al. (2004), are plotted. In panels *b* and *c*, galaxies in the SFB and WFB models are plotted, respectively. Among galaxies satisfying the above criterion, we randomly pick out galaxies so as to show almost the same number of galaxies as that of the GOODS samples. The solid lines indicate evolutionary tracks of single stellar populations of the solar metallic-

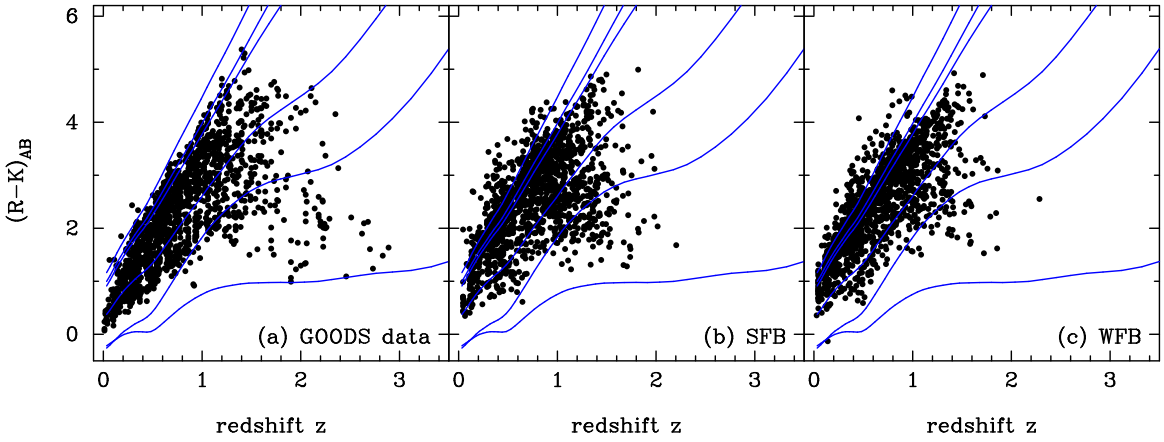

FIG. 24.— Color-redshift diagram for the (a) GOODS galaxies, (b) SFB model, and (c) WFB model. The color $(R-K)_{AB}$ is defined in the observer frame. The observed data are taken from Figure 2 in Somerville et al. (2004). In panels *b* and *c*, we randomly pick out galaxies of $K_{AB} < 22 - 0.2$, where 0.2 means the correction to obtain the isophotal magnitude, from the mock catalogs based on the SFB and WFB models in order to be a number similar to the GOODS samples. The solid lines indicate evolutionary tracks of single stellar populations of solar metallicity with ages of 13.5, 5.8, 3.2, 1, 0.5, and 0.1 Gyr, from the top to the bottom, computed using the model given by Kodama & Arimoto (1997). These ages are the same as those in Figure 2 of Somerville et al. (2004), selected for ease of comparison.

ity with ages of 13.5, 5.8, 3.2, 1, 0.5, and 0.1 Gyr, from the top to the bottom, estimated using the model given by Kodama & Arimoto (1997). These ages are the same as those in Figure 2 of Somerville et al. (2004) so that we can easily compare our results with theirs. As can be seen, both the SFB and WFB models are in good agreement with the GOODS survey. Somerville et al. (2004) has concluded that their SA model broadly agrees with the GOODS survey, while a small discrepancy remains insofar as their SA model does not produce enough galaxies with very red colors, $(R-K)_{AB} \gtrsim 4$, at $z \sim 0.8 - 1.2$. Our models seem to be able to produce more red galaxies, but slight discrepancies also remain. As shown below, one of these is the lack of galaxies with $(R-K)_{AB} \sim 2$ at $z \sim 2.5$, and another is the existence of too many galaxies above the 13.5 Gyr single stellar population line. A key to understanding the evolution of colors should be dust extinction. Our SA model has two types of dust extinction associated with the two modes of star formation, quiescent disk star formation and starbursts. By switching on and off the dust extinction, we investigate the effects of dust on colors.

Here we examine the effects of dust extinction for starbursts. As explained in §§2.7, the SF time-scale for starbursts, $\tau_{\rm burst}$, is assumed to be equal to the dynamical time-scale of the spheroidal component, $t_{\rm dyn} \equiv r_e/V_b$. Firstly we change this relation to $\tau_{\rm burst} = 0.5 t_{\rm dyn}$, that is, we take half the dynamical time-scale as the SF time-scale for starbursts. In panels *a* and *b* of Figure 25, we show the same as Figure 24, but for the above short starburst time-scale for the SFB and WFB models, respectively. It is evident that, in both models, many galaxies with $(R-K)_{AB} \sim 2$ at $z \sim 2$ emerge and therefore the agreement with the observation is much improved, though not perfect. The reason for this improvement is explained as follows: The time-scale of starbursts in our SA model is distributed in a broad range comparable to the time-step, about 0.3-0.5 Gyr, at low redshift. Right after starbursts, the age effect on the luminosity, even for such a short time-scale, is significant, so we put the epoch of starbursts within the time-step randomly, depending on the merger time-scale. Therefore, for some galaxies, starbursts happen just before the output redshift. Such galaxies just after starbursts are expected to be intrinsically very blue. When the SF time-scale for starbursts becomes shorter, the amount of dust estimated from the amount of cold gas and metals becomes smaller at the output redshift. Thus, by shortening the SF time-scale for starbursts, several blue galaxies emerge.

This can be clearly seen if we do not include the dust extinction for starbursts at all. In the center panels *c* and *d* of Figure 25, we show the same models as the SFB and WFB models but without dust extinction during starburst phases ('bare' starbursts). At high redshift $z \gtrsim 1$, very blue galaxies with $(R-K)_{AB} \lesssim 0$ emerge in both the SFB and WFB models. These galaxies are those just after starbursts. The GOODS data at such a high redshift suggest that clearly starbursts should not be bare, but our dust model for starbursts might be too strong. We have also tried the slab dust model instead of the screen dust model, but found that it does not work well. It should also be noted that dust extinction can remove galaxies from this figure because galaxies do not satisfy the selection criterion, $K_{AB} + 0.2 < 22$. More sophisticated modeling of dusty starbursts would be required in future.

Next, we discuss the extinction of disk luminosities. In the right panels *e* and *f* of Figure 25, we show the same models as the SFB and WFB models, but without any dust extinction. By this manipulation, galaxies above the line of single stellar populations of 13.5 Gyr disappear, similar to the GOODS data. This might suggest that our dust model for disks is stronger than the observed galaxies. Part of the reason should be the higher value of the chemical yield we use, because the optical depth is proportional to the metallicity of cold gas, as mentioned in §§4.5. Presumably, careful choice of IMFs, which determine the chemical yield, depending on the SF mode will improve the color distribution.

It should be noted that the changing of the optical depth for disks may affect various observables. For example, weakening the dust extinction in a simple way would cause overestimation of faint galaxy counts in optical pass-bands. In order to obtain full agreement after changing the optical depth, therefore, a new set of model parameters will be required. Instead, if the extinction only for strongly reddened galaxies is weakened, it might not significantly affect model parameters. The change of γ might also recover the agreement with the ob-

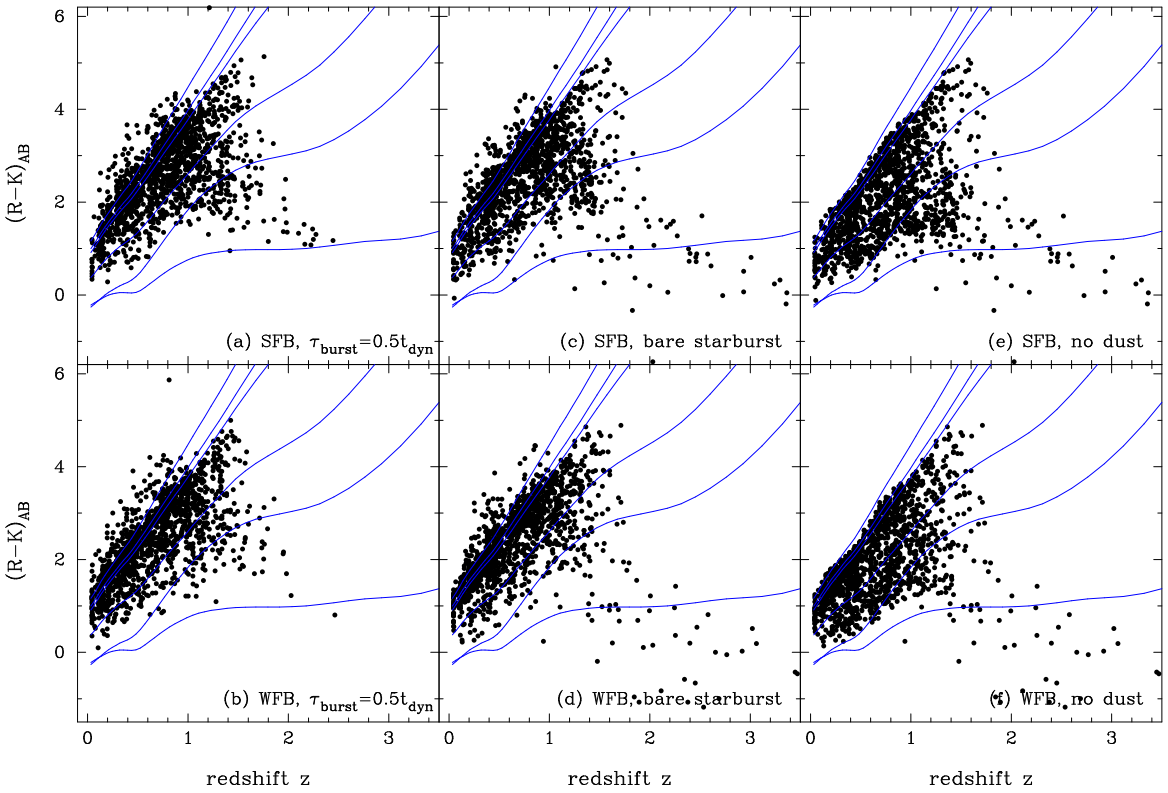

FIG. 25.— Color-redshift diagram for the (a) SFB and (b) WFB models with $\tau_{\rm burst} = 0.5t_{\rm dyn}$, the (c) SFB and (d) WFB models with no dust extinction during starbursts, and the (e) SFB and (f) WFB models with no dust extinction at all. The solid lines are the same as those in Figure 24.

servational galaxy counts. In all cases, the dust model adopted in this paper is very simple and should be refined in future. By contrast, the dust model for starbursts is not the case because the number fraction of bursting galaxies is smaller than that of normal galaxies. As shown in the next subsection, however, it might affect the number of high redshift galaxies at $z \gtrsim 3$, at which a substantial fraction of stars is formed via starbursts, while the contribution to faint galaxy counts is small.

5.5. *Cosmic Star Formation Histories*

Recently the cosmic SF history, which is a plot of SFRs in a comoving volume against redshift, has been recognized as one of the fundamental quantities characterizing galaxy formation (Madau et al. 1996), in spite of large uncertainties in its estimation caused by, for example, dust obscuration and shape of the luminosity function below the detection limit. Figure 26 shows the cosmic SFR as a function of redshift. The solid and dashed lines represent the SFB and WFB models, respectively. For comparison, the Mitaka CSF model, in which the SF time-scale is independent of redshift similar to the SFB and WFB models, is also plotted by the dotted line. Symbols are the observational data from surveys indicated in the figure. Note that the observational values are corrected, taking into account dust extinction, and also that there are still large uncertainties originating in undetected faint galaxies at high redshift. As shown in Figure 21 of Ouchi et al. (2004), observationally obtained cosmic SFRs strongly depend on the assumed luminosity function, which is guessed from the data for detected bright galaxies. The upper limits for values at $z \gtrsim 3$ estimated by Ouchi et al. (2004) are about a factor of two larger than plotted values. These are obtained by integrating luminosity functions down to the luminosity $L = 0$.

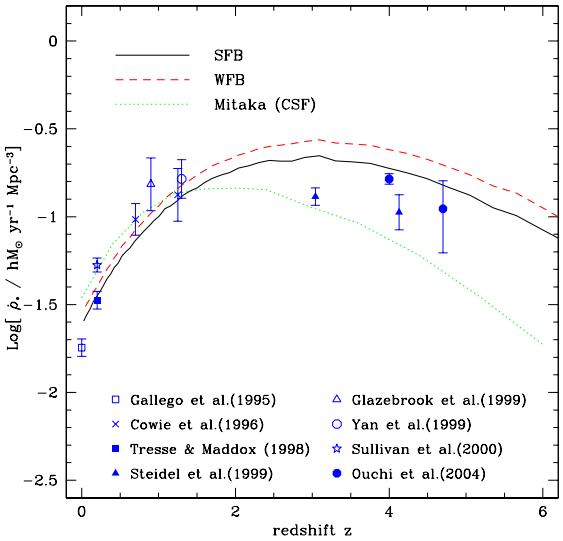

FIG. 26.— Cosmic SF histories. The solid and dashed lines represent the SFB and WFB models, respectively. For reference, the Mitaka CSF model in NY04 is also plotted by the dotted line. Symbols with error bars are the observed cosmic SFRs as indicated in the figure.

Taking into account such uncertainties which are not included in plotted error bars, the SFB and WFB models are in good agreement with the observations.

As we have already shown in NY04, the cosmic SFR strongly depends on the model of the SF time-scale. If the SF time-scale becomes shorter toward higher redshift, for example, proportional to the dynamical time-scale of disks or

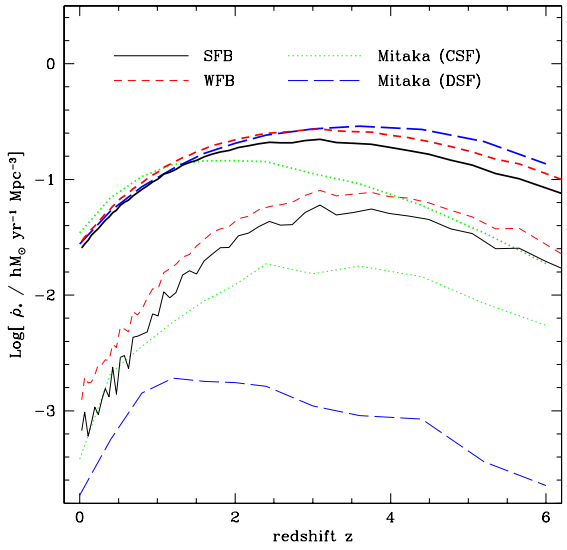

FIG. 27.— Cosmic SF histories. The solid and short dashed lines represent the SFB and WFB models, respectively. The dotted and long dashed lines represent the Mitaka CSF and DSF models, respectively, in NY04. The thick lines indicate the total SFR, and the thin lines the SFR only for starbursts.

halos, the peak of the cosmic SFR moves to a higher redshift. Because the SFB and WFB models have the same SF model, which is independent of redshift, their predicted cosmic SFRs are similar. The Mitaka CSF model, however, shows different cosmic SFRs, in spite of having the same redshift dependence as the SF time-scale. This would suggest that it is very important for high redshift galaxies to correctly estimate merging histories of dark halos, as pointed out in §§5.2.

Figure 27 shows not only the total cosmic SFR (*thick lines*) but also the SFR only for starbursts (*thin lines*). The solid and short dashed lines represent the SFB and WFB models, respectively. The dotted and long dashed lines represent the Mitaka CSF and DSF models, respectively. The former has a SF time-scale independent of redshift, and the latter a SF time-scale proportional to the dynamical time-scale of dark halos, which becomes shorter toward higher redshift. Although the total cosmic SFRs of the SFB and WFB models are similar to the Mitaka DSF model rather than the Mitaka CSF model, SFRs for starbursts are quite different. The SFB and WFB models predict a very large contribution of starbursts to the total SFR up to 15-20% at $z \sim 2$ and 25-30% at $z \sim 4$, while the Mitaka CSF model predicts a contribution of starbursts about 10% at $z \sim 2$ and 20% at $z \sim 4$ and the Mitaka DSF model at most 2% at $z \sim 1$. If the IMF for starbursts is top-heavy, as suggested by Baugh et al. (2005) and Nagashima et al. (2005a), this significant fraction would affect many aspects, such as the chemical enrichment and the cosmic rates of supernovae and γ-ray bursts.

6. SUMMARY

We have developed a semi-analytic (SA) model combined with high resolution N-body simulations, which we call the *Numerical Galaxy Catalog* (νGC). The minimum mass of dark halos is down to $3.04\times10^9 M_\odot$, which corresponds to $V_{\rm circ} \sim 20$ km s^{-1} at $z = 0$ and 40 km s^{-1} at $z \simeq 4$. These are enough to resolve the effective Jeans mass, or the filtering mass, after the cosmic reionization. To examine the effects of the resolution on galaxy formation, we also used another simulation with a box twice the size, in which the minimum mass of dark halos is $2.43 \times 10^{10} M_\odot$ corresponding to $V_{\rm circ} \sim 40$ km s^{-1} and 80 km s^{-1}. Although this resolution is not significantly worse among the currently available cosmological N-body simulations, we have found that it alters luminosity functions, especially the faint-end slope. Because SN feedback-related parameters ($\alpha_{\rm hot}$ and $V_{\rm hot}$) are determined so as to match luminosity functions, worse resolutions should affect values of parameters. We would like to stress that the resolution of our SA model is much better than that of currently available data provided by SA models combined with N-body simulations in the public domain. For example, the particle mass of dark matter in the GIF project (Kauffmann et al. 1999a) is about 65 times larger than ours, and that of the GalICS project (Hatton et al. 2003) is about 27 times larger. These are even worse than our 140 h^{-1} Mpc box simulation.

Within observational uncertainties of the shape of luminosity functions, we have adopted two parameter sets. One is the strong SN feedback (SFB) model and another is the weak SN feedback (WFB) model. In this paper, we have focused on comparison of these models with photometric, structural, and kinematical properties of observed galaxies. Both models reproduce many observations well, and we slightly prefer the SFB model to the WFB model. Below, we summarize the results.

1. We have explicitly shown that both the SFB and WFB models are in reasonable agreement with the following observational results: luminosity functions in B and K bands, cold gas mass-to-B band luminosity ratios of spiral galaxies, H I mass functions, size-magnitude relations for spiral and elliptical galaxies, and the Faber-Jackson relation at $z = 0$, and faint galaxy number counts in $BVRi'z'$ bands, isophotal area, and cosmic star formation histories at high redshift. Note that some of the above observations were used to fix the model parameters. For example, the SN feedback-related parameters were determined by matching the luminosity functions. Table 3 summarizes observations to fix the parameters.

2. The SFB model is in broad agreement with the observed galaxy counts in the near-infrared K' band. Most observed redshift distributions also are broadly reproduced by the SFB model, except for the faintest galaxies ($23 < K' \leq 24$) in the Subaru Deep Survey, while the results are much improved compared with those of the Mitaka model based on the analytic EPS formalism, not on N-body simulations. However, since errors caused by uncertainties in estimating photometric redshifts are very large for such faint galaxies, this discrepancy may not be taken so seriously. Future observations with accurate determination of redshifts and with a large survey area will provide sufficiently better redshift distributions for very faint galaxies to make clear whether models are in agreement with observations or not. By contrast, the WFB model is not consistent with the observed K' band galaxy counts in the Subaru Deep Field, while it is in agreement with optical ($BVRi'z'$) galaxy counts. This model is also inconsistent with redshift distributions, in particular, for faint galaxies.

3. The Tully-Fisher (TF) relation slightly favors the WFB model to the SFB model, because the slope of the TF relation predicted by the SFB model is steeper than the observed one. This contradiction in the TF relation may be improved if we

introduce dynamical response on the rotation velocity to gas removal induced by the SN feedback, which is only taken into account for starbursts making spheroidal systems in the current model. We are going to explicitly consider this effect on spiral galaxies in future.

4. The bright end of color-magnitude relations of cluster elliptical galaxies in the SFB and WFB models is almost flat against magnitudes and also inconsistent with observations. Presumably, this will be amended by adopting different IMFs for disk star formation and starbursts. Introducing the chemical enrichment due to SNe Ia into the Mitaka model, Nagashima & Okamoto (2004) have shown that chemical yields consistent with Salpeter's IMF are in agreement with observed metallicities and their ratios in the solar neighborhood. Moreover, Nagashima et al. (2005a) have also shown that metallicities of the intracluster medium can be reproduced only when adopting a top-heavy IMF for starbursts and Kennicutt's IMF for disk star formation. Therefore it is not unreasonable to adopt different IMFs. At this stage, however, it is beyond the scope of this paper.

5. Both models predict $(R-K)_{AB}$ colors against redshifts broadly consistent with the observational GOODS galaxies. Particularly, our models are able to produce red galaxies $(R-K)_{AB} \sim 5$, which have not been reproduced by an SA model of the GOODS group (Somerville et al. 2004). However, slight discrepancies remain. One is lack of galaxies with $(R-K)_{AB} \sim 1-2$ at $z \gtrsim 2$. If we switch off the dust extinction for starburst galaxies, several galaxies emerge. At the same time, however, very blue galaxies with $(R-K)_{AB} \lesssim 1$ also emerge. When a shorter star formation time-scale is used for starbursts similar to half the dynamical time-scale, the situation can be improved. This means that more sophisticated modeling of dusty starbursts should be required. Second is that our model produces excessively red galaxies at low redshift, $z \lesssim 1$. This is caused by too strong a dust extinction for disk stars. This might suggest that the chemical yield used here, which is almost twice the solar metallicity, is too large, because dust optical depth is proportional to the metallicity of cold gas. This high value is required to produce red elliptical galaxies to be consistent with observed cluster ellipticals. Therefore, similar to color-magnitude relations, adopting different IMFs for disk star formation and starbursts will help these galaxies become blue.

This is a first paper in a series of νGC. Subsequent papers will discuss clustering properties of spatial distribution of galaxies (Yahagi et al. 2005). We also plan to combine the quasar formation model given by Enoki, Nagashima & Gouda (2003) with this model (Enoki et al. 2005). νGC will be a useful tool with which to understand galaxy formation in studies of various current and future large galaxy surveys.

We would like to thank Takashi Okamoto for useful comments on modeling galaxy formation with N-body simulations, Nobunari Kashikawa for useful discussion on the Subaru Deep Survey, Bahram Mobasher for providing the GOODS data of redshift distribution plotted in Figure 22, Masami Ouchi for providing the data of cosmic SFRs plotted in Figure 26, and Katsuya Okoshi for useful discussion on H I mass functions. This work has been supported in part by the Grant-in-Aid for the Center-of-Excellence research (07CE2002) of the Ministry of Education, Science, Sports and Culture of Japan. MN acknowledges support from the PPARC rolling grant for extragalactic astronomy and cosmology at Durham and from the Japan Society for the Promotion of Science for Young Scientists (No.207). N-body simulations described in this paper were carried out using Fujitsu-made vector parallel processors VPP5000 installed at the Astronomical Data Analysis Center, National Astronomical Observatory, Japan (ADAC/NAOJ), under the ADAC/NAOJ large scale simulation projects (group-ID: myy26a, yhy35b).

REFERENCES

Arimoto, N., & Yoshii, Y. 1986, A&A, 164, 260
Arimoto, N., & Yoshii, Y. 1987, A&A, 173, 23
Bardeen, J. M., Bond, J. R., Kaiser, N., & Szalay, A. S. 1986, ApJ, 304, 15
Baugh, C. M., Cole, S., & Frenk, C. S. 1996, MNRAS, 283, 1361
Baugh, C. M., Cole, S., Frenk, C. S., & Lacey, C. G. 1998, ApJ, 498, 504
Baugh, C. M., Lacey, C. G., Frenk, C. S., Granato, G. L., Silva, L., Bressan, A., Benson, A. J., & Cole, S. 2005, MNRAS, 356, 1191
Bell, E. F., McIntosh, D. H., Katz, N., & Weinberg, M. D. 2003, ApJS, 149, 289
Bender, R., Burstein, D., & Faber, S. M. 1992, ApJ, 399, 462
Benson, A.J., Bower, R. G., Frenk, C.S., Lacey, C. G., Baugh, C.M., & Cole, S. 2003, ApJ, 599, 38
Benson, A.J., Cole, S., Frenk, C.S., Baugh, C.M., & Lacey, C.G. 2000, MNRAS, 311, 793
Benson, A.J., Frenk, C.S., Baugh, C.M., Cole, S., & Lacey, C.G. 2001, MNRAS, 327, 1041
Binney, J., & Tremaine, S. 1987, Galactic Dynamics, Princeton Univ. Press, Princeton, NJ
Bond, J. R., Cole, S., Efstathiou, G., & Kaiser, N. 1991, ApJ, 379, 440
Bower, R. 1991, MNRAS, 248, 332
Bower, R., Lucey, J.R., & Ellis, R.S. 1992, MNRAS, 254, 601
Bullock, J.S., Kolatt, T.S., Sigad, T., Somerville, R.S., Kravtsov, A.V., Klypin, A.A., Primack, J.R., & Dekel, A. 2001, MNRAS, 321, 559
Catelan, P., & Theuns, T. 1996a, MNRAS, 282, 436
Catelan, P., & Theuns, T. 1996b, MNRAS, 282, 455
Cen, R., & Ostriker, J. P. 1999, ApJ, 514, 1
Cole, S., Aragon-Salamanca, A., Frenk, C. S., Navarro, J. F., & Zepf, S. E. 1994, MNRAS, 271, 781
Cole, S., Lacey, C. G., Baugh, C. M., & Frenk, C. S. 2000, MNRAS, 319, 168
Cole, S. et al. 2001, MNRAS, 326, 255
Cowie, L. L., Songaila, A., Hu, E. M., & Cohen, J. G. 1996, AJ, 112, 839
Davis, M., Efstathiou, G., Frenk, C.S., & White, S.D.M. 1985, ApJ, 292, 371
Diaferio, A., Kauffmann, G., Colberg, J.M., & White, S.D.M. 1999, MNRAS, 307, 537
Diaferio, A., Kauffmann, G., Balogh, M.L., White, S.D.M., Schade, D., & Ellingson, E. 2001, MNRAS, 323, 999
Disney, M., Davies, J., & Phillipps, S. 1989, MNRAS, 239, 939
Dressler, A. 1980, ApJ, 236, 351
Enoki, M., Nagashima, M., & Gouda, N. 2003, PASJ, 55, 133
Enoki, M., Inoue, K. T., Nagashima, M., & Sugiyama, N. 2004, ApJ, 615, 19
Enoki, M., Yahagi, H., Nagashima, M., Gouda, N., & Yoshii, Y. 2005, in preparation
Faber, S. M., & Jackson, R. E. 1976, ApJ, 204, 668
Fall, S. M. 1979, Nature, 281, 200
Fall, S. M., & Efstathiou, G. 1980, MNRAS, 193, 189
Fall, S. M. 1983, in 'Internal kinematics and dynamics of galaxies', proceedings of the IAU symposium 100, Besancon, France, Dordrecht, D. Reidel, p.391
Folkes, S. et al. 1999, MNRAS, 308, 459
Furusawa, H., Shimasaku, K., Doi, M., & Okamura, S. 2000, ApJ, 534, 624
Gallego, J., Zamorano, J., Aragón-Salamanca, A., & Rego, M. 1995, ApJ, 455, L1
Gardner, J. P., Sharples, R. M., Carrasco, B. E., & Frenk, C. S. 1996, MNRAS, 282, L1
Garnett, D. 2002, ApJ, 581, 1019
Giovanelli, R., Haynes, M.P., da Costa, L.N., Freudling, W., Salzer, J.J., & Wegner, G. 1997, ApJ, 477, L1
Glazebrook, K., Blake, C., Economou, F., Lilly, S., & Colles, M. 1999, MNRAS, 306, 843

Glazebrook, K., Peacock, J.A., Miller, L., & Collins, C.A. 1994, MNRAS, 266, 65
Gnedin, N. Y. 2000, ApJ, 542, 535
Gunn, J.E., & Gott, J.R. 1972, ApJ, 176, 1
Hatton, S., Devriendt, J. E. G., Ninin, S., Bouchet, F. R., Guiderdoni, B., & Vibert, D. 2003, MNRAS, 343, 75
Helly, J. C., Cole, S., Frenk, C. S., Baugh, C. M., Benson, A. J., & Lacey, C. 2003a, MNRAS, 338, 903
Helly, J. C., Cole, S., Frenk, C. S., Baugh, C. M., Benson, A. J., Lacey, C., & Pearce, F. R. 2003b, MNRAS, 338, 913
Huang, J.-S., Glazebrook, K., Cowie, L. L., & Tinney, C. 2003, ApJ, 584, 203
Huchtmeier, W. K., & Richter, O. -G. 1988, A&A, 203, 237
Impey, C.D., Sprayberry, D., Irwin, M. J., & Bothun, G. D. 1996, ApJS, 105, 209
Inoue, S., Nagashima, M., Suzuki, T. K., & Aoki, W. 2004, JKAS, 37, 447
Jaffe, W. 1983, MNRAS, 202, 995
Jenkins, A., Frenk, C. S., White, S. D. M., Colberg, J. M., Cole, S., Evrard, A. E., Couchman, H. M. P., & Yoshida, N. 2001, MNRAS, 321, 372
Kashikawa, N., et al. 2003, AJ, 125, 53
Kashikawa, N., et al. 2004, PASJ, 56, 1011
Kauffmann, G., Colberg, J.M., Diaferio, A., & White, S.D.M. 1999a, MNRAS, 303, 188
Kauffmann, G., Colberg, J.M., Diaferio, A., & White, S.D.M. 1999b, MNRAS, 307, 529
Kauffmann, G., & Charlot, S. 1998, MNRAS, 294, 705
Kauffmann, G., & Haehnelt, M. 2000, MNRAS, 311, 576
Kauffmann, G., & White, S. D. M. 1993, MNRAS, 261, 921
Kauffmann, G., White, S. D. M., & Guiderdoni, B. 1993, MNRAS, 264, 201
Knebe, A., Green, A., & Binney, J. 2001, MNRAS, 325, 845
Kochanek, C.S. et al. 2001, ApJ, 560, 566
Kodama, T., & Arimoto, N. 1997, A&A, 320, 41
Kodama, T., Arimoto, N., Barger, A.J., & Aragón-Salamanca A.1998, A&A, 334, 99
Kravtsov, A.V., Klypin, A.A., Khokhlov, A.M. 1997, ApJS, 111, 73
Lacey, C.G., & Cole, S. 1993, MNRAS, 262, 627
Loveday, J., Peterson, B. A., Efstathiou, G., & Maddox, S. J. 1992, ApJ, 90, 338
Madau, P. 1995, ApJ, 441, 18
Madau, P., Ferguson, H. C., Dickinson, M. E., Giavalisco, M., Steidel, C. C., & Fruchter, A. 1996, MNRAS, 283, 1388
Maeder, A. 1992, A&A, 264, 105
Maihara, T. et al. 2001, PASJ, 53, 25
Makino, J., & Hut, P. 1997, ApJ, 481, 83
Mamon, G. A. 2000, ASP conf. series, Vol.197, pp.377 (astro-ph/9911333)
Mathewson, D.S., Ford, V.L., & Buchhorn, M. 1992, ApJS, 81, 413
McLeod, B.A., Bernstein, G.M., Rieke, M.J., Tollestrup, E.V., & Fazio, G.G. 1995, ApJS, 96, 117
Menci, N., Cavaliere, A., Fontana, A., Giallongo, E., & Poli, F. 2002, ApJ, 575, 18
Minezaki, T., Kobayashi, Y., Yoshii, Y., & Peterson, B.A. 1998, ApJ, 494, 111
Mo, H.J., Mao, S., & White, S.D.M. 1998, MNRAS, 295, 319
Monaco, P. 1998, Fundam. Cosmic Phys., 19, 157
Mori M., Yoshii Y., Tsujimoto T., Nomoto K., 1997, ApJL, 478, L21
Mori M., Yoshii Y., Nomoto K., 1999, ApJ, 511, 585
Nagashima, M. 2001, ApJ, 562, 7
Nagashima, M., & Gouda, N. 1997, MNRAS, 287, 515
Nagashima, M., & Gouda, N. 1998, MNRAS, 301, 849
Nagashima, M., Gouda, N., & Sugiura, N. 1999, MNRAS, 305, 449
Nagashima, M., & Gouda, N. 2001, MNRAS, 325, L13
Nagashima, M., Lacey, C. G., Baugh, C. M., Frenk, C. S., & Cole, S. 2005, MNRAS, 358, 1247
Nagashima, M., Lacey, C. G., Okamoto, T., Baugh, C. M., Frenk, C. S., & Cole, S. 2005, MNRAS, in press (astro-ph/0504618)
Nagashima, M., & Okamoto, T. 2004, submitted.
Nagashima, M., Totani, T., Gouda, N., & Yoshii, Y. 2001, ApJ, 557, 505
Nagashima, M., Yoshii, Y., Totani, T., & Gouda, N. 2002, ApJ, 578, 675
Nagashima, M., & Yoshii, Y. 2003, MNRAS, 340, 509
Nagashima, M., & Yoshii, Y. 2004, ApJ, 610, 23 (NY04)
Nicastro, F. et al. 2005, Nature, 433, 495
Okamoto, T., Eke, V. R., Frenk, C. S., & Jenkins, A. 2005, preprint (astro-ph/0503676)
Okamoto, T., Jenkins, A., Eke, V. R., Quilis, V., & Frenks, C. S. 2003, MNRAS, 345, 429
Okamoto, T., & Habe, A. 1999, ApJ, 516, 591
Okamoto, T., & Habe, A. 2000, PASJ, 52, 457
Okamoto, T., & Nagashima, M. 2001, ApJ, 547, 109
Okamoto, T., & Nagashima, M. 2003, ApJ, 587, 500
Okoshi, K., Nagashima, M., Gouda, N., & Yoshioka, S. 2004, ApJ, 603, 12
Ouchi, M., et al. 2004, ApJ, 611, 660
Peacock, J. A., & Heavens, A. F. 1990, MNRAS, 243, 133
Peebles, P. J. E. 1969, ApJ, 155, 393
Perlmutter, S., et al. 1999, ApJ, 517, 565
Pierce, M., & Tully, R.B. 1992, ApJ, 387, 47
Press, W., & Schechter, P. 1974, ApJ, 187, 425
Ratcliffe, A., Shanks, T., Parker, Q., & Fong, R. 1998, MNRAS, 293, 197
Reed, D., Gardner, J., Quinn, T., Stadel, J., Fardal, M., and Lake, G. 2003, MNRAS, 346, 565
Riess, A. G., et al. 1998, AJ, 116, 1009
Rosenberg, J. L., & Schneider, S. E. 2002, ApJ, 567, 247
Roukema, B.F., Peterson, B.A., Quinn, P.J., & Rocca-Volmerange, B. 1997, MNRAS, 292, 835
Sage, L. J. 1993, A&A, 272, 123
Salpeter, E. E. 1955, ApJ, 121, 161
Seaton, M. J. 1979, MNRAS, 187, 73P
Sheth, R., & Tormen, G. 1999, MNRAS, 308, 119
Shimizu, M., Kitayama, T., Sasaki, S., & Suto, Y. 2002, PASJ, 54, 645
Simard, L., Koo, D. C., Faber, S. M., Sarajedini, V. L., Vogt, N. P., Phillips, A. C., Gebhardt, K., Illingworth, G. D., & Wu, K. L. 1999, ApJ, 519, 563
Simien, F., & de Vaucouleurs, G. 1986, ApJ, 302, 564
Somerville, R.S., & Kolatt, T. 1999, MNRAS, 305, 1
Somerville, R.S., Lemson, G., Sigad, Y., Dekel, A., Kauffmann, G., & White, S.D.M. MNRAS, 320, 289
Somerville, R. S. 2002, ApJ, 572, L23
Somerville, R. S., et al. 2004, ApJ, 600, L135
Somerville, R. S., & Primack, J. R. 1999, MNRAS, 310, 1087
Spergel, D.N. et al. 2003, ApJS, 148, 175
Springel, V., White, S.D.M., Tormen, G., & Kauffmann, G. 2001, MNRAS, 328, 726
Steidel, C. C., Adelberger, K. L., Giavalisco, M., Dickinson, M., & Pettini, M. 1999, ApJ, 519, 1
Sugiyama, N. 1995, ApJS, 100,281
Sullivan, M., Treyer, M. A., Ellis, R. S., Bridges, T. J., Milliard, B., & Donas, J. 2000, MNRAS, 312, 442
Sutherland, R., & Dopita, M. A. 1993, ApJS, 88, 253
Teyssier, R., 2002 A&A, 385, 337
Tomita, K. 1969, Prog. Theor. Phys., 42, 9
Totani, T., & Yoshii, Y. 2000, ApJ, 540, 81
Totani, T., Yoshii, Y., Maihara, T., Iwamuro, F., & Motohara, K. 2001, ApJ, 559, 592
Tresse, L., & Maddox, S. J. 1998, ApJ, 495, 691
Tully, R. B., & Fisher, J. R. 1977, A&A, 54, 661
van Kampen, E., Jimenez, R., & Peacock, J. A. 1999, MNRAS, 310, 43
White, M. 2002, ApJS, 143, 241
White, S.D.M. 1984, ApJ, 286, 38
Williams, R. T. et al. 1996, AJ, 112, 1335
Yahagi, H. 2005, PASJ, 57, in press (astro-ph/0507339)
Yahagi, H., Nagashima, M., Enoki, M., Gouda, N., & Yoshii, Y. 2005, in preparation
Yahagi, H., Nagashima, M., & Yoshii, Y. 2004, ApJ, 605, 709
Yahagi, H., & Yoshii, Y. 2001, ApJ, 558, 463
Yan, L., McCarthy, P. J., Freudling, W., Teplitz, H. I., Malumuth, E. M., Weymann, R. J., & Malkan, M. A. 1999, ApJ, 519, L47
Yano, T., Nagashima, M., & Gouda, N. 1996, ApJ, 466, 1
Yoshii, Y. 1993, ApJ, 403, 552
Yoshii, Y., & Arimoto, N. 1987, A&A, 188, 13
Yoshii, Y., & Peterson, B. A. 1994, ApJ, 436, 551
Yoshii, Y., & Takahara, F. 1988, ApJ, 326, 1
Yoshikawa, K. et al. 2004, PASJ, 56, 939
Zucca, E. et al. 1997, A&A, 326, 477
Zwaan, M. A. et al. 2003, AJ, 125, 2842